Geophysical Journal International

Geophys. J. Int. (2022) **229,** 1604–1627
Advance Access publication 2022 January 18
GJI Marine Geosciences and Applied Geophysics

https://doi.org/10.1093/gji/ggac019

Active ocean–continent transform margins: seismic investigation of the Cayman Trough-Swan Island ridge-transform intersection

C. Peirce [1], I. Grevemeyer [2], N.W. Hayman[3] and H.J.A. Van Avendonk[4]

[1] *Department of Earth Sciences, Durham University, South Road, Durham DH13LE, UK. E-mail: christine.peirce@durham.ac.uk*
[2] *GEOMAR Helmholtz Centre for Ocean Research, 24148 Kiel, Germany*
[3] *Oklahoma Geological Survey, University of Oklahoma,* 100 *E. Boyd Street, Norman, OK 73019, USA*
[4] *Institute for Geophysics, Jackson School of Geosciences, University of Texas, Austin, TX 78712, USA*

Accepted 2022 January 14. Received 2022 January 10; in original form 2021 October 19

SUMMARY

The southern boundary of the Cayman Trough in the Caribbean is marked by the Swan Islands transform fault (SITF), which also represents the ocean–continent transition of the Honduras continental margin. This is one of the few places globally where a transform continental margin is currently active. The *CAYSEIS* experiment acquired an ∼165-km-long seismic refraction and gravity profile (P01) running across this transform margin, and along the ridge-axis of the Mid-Cayman Spreading Centre (MCSC) to the north. This profile reveals not only the crustal structure of an actively evolving transform continental margin, that juxtaposes Mesozoic-age continental crust to the south against zero-age ultraslow spread oceanic crust to the north, but also the nature of the crust and uppermost mantle beneath the ridge-transform intersection (RTI). The traveltimes of arrivals recorded by ocean-bottom seismographs (OBSs) deployed along-profile have been inverse and forward modelled, in combination with gravity modelling, to reveal an ∼25-km-thick continental crust that has been continuously thinned over a distance of ∼65 km to ∼10 km adjacent to the SITF, where it is juxtaposed against ∼3–4-km-thick oceanic crust. This thinning is primarily accommodated within the lower crust. Since Moho reflections are only sparsely observed, and, even then, only by a few OBSs located on the continental margin, the 7.5 km s^{-1} velocity contour is used as a proxy to locate the crust–mantle boundary along-profile. Along the MCSC, the crust–mantle boundary appears to be a transition zone, at least at the seismic wavelengths used for *CAYSEIS* data acquisition. Although the traveltime inversion only directly constrains the upper crust at the SITF, gravity modelling suggests that it is underlain by a higher density (>3000 kg m^{-3}) region spanning the width (∼15 km) of its bathymetric expression, that may reflect a broad region of metasomatism, mantle hydration or melt-depleted lithospheric mantle. At the MCSC ridge-axis to the north, the oceanic crust appears to be forming in zones, where each zone is defined by the volume of its magma supply. The ridge tip adjacent to the SITF is currently in a magma rich phase of accretion. However, there is no evidence for melt leakage into the transform zone. The width and crustal structure of the SITF suggests its motion is currently predominantly orthogonal to spreading. Comparison to *CAYSEIS* Profile P04, located to the west and running across-margin and through 10 Ma MCSC oceanic crust, suggests that, at about this time, motion along the SITF had a left-lateral transtensional component, that accounts for its apparently broad seabed appearance westwards.

Key words: Controlled source seismology; Continental margins: transform; Crustal structure; Oceanic transform and fracture zone processes.

1 INTRODUCTION

Large-scale transform faults and fracture zones are observed to segment passive rifted margins globally, but such transform ocean–continental margins are infrequently studied and are much less well understood than their rifted equivalents. Along many margins, the continental crust is juxtaposed against oceanic crust across a transform-fracture system which is generally traceable to a corresponding offset in the global mid-ocean ridge system. Characteristically, within the ocean–continent transition (OCT—Sage *et al.*

2000), the adjacent continental slope is steep and associated with an elevated marginal ridge basement surface (Francheteau & Le Pichon 1972; Mascle 1976). These pronounced bathymetric ridges are, variously, explained by the contrast in heat flow between adjacent old cold continental and young hot oceanic lithosphere (Todd *et al.* 1988; Lorenzo & Vera 1992; Gadd & Scrutton 1997), compressional tectonics (Blarez & Mascle 1988) and rapid variation in subsidence and/or magmatic underplating (Basile *et al.* 1998).

Ocean–continent transforms are thought to initiate by ridge jumps after rifting (e.g. Taylor *et al.* 2009), since they can accommodate very large offsets that ultimately lead to large-scale plate reorganizations (Dalziel & Dewey 2019). However, little is known about their active stages of development, how the oceanic and continental lithosphere are mechanically and thermally coupled, the nature of the magmatic processes occurring at the adjacent spreading centre tip, nor if magmatism occurs within the active transform. Conversely, transform faults are also thought to be sites of significant mantle hydration (White *et al.* 1984), where the resulting serpentinite may facilitate large-scale slip by fault weakening (Escartín *et al.* 1997).

In relatively few locations globally, the deep structure of transform margins has been modelled with both gravity and wide-angle seismic refraction data (e.g. Edwards *et al.* 1997; Greenroyd *et al.* 2008; Peirce *et al.* 2019b), with the majority of the studies focusing on relict inactive margins (Stage 3—Mascle & Blarez 1987; Peirce *et al.* 1996; Mascle *et al.* 1997; Greenroyd *et al.* 2007—and summarized in fig. 1 of Peirce *et al*. 2019b), where active lateral motion has ceased and a thick layer of sediments covers the igneous basement (e.g. Christeson *et al.* 2010).

Detrick *et al.* (1993) view large-offset transform faults as being heterogeneous in both thickness and internal structure, with the surrounding crust being quite thin (<1–2 km thick), having a low *P*-wave velocity, and without a traditional oceanic layer 3 (gabbroic layer). The accepted interpretation of the limited existing observations (e.g. White *et al.* 1984; Müller *et al.* 2000; Kuna *et al.* 2019; Peirce *et al.* 2019a,b) is that transform crust comprises a thin, intensely fractured, and hydrothermally altered basaltic section overlying extensively serpentinized ultramafics. A reduced magma supply at the mid-ocean ridge-transform intersection (Tolstoy *et al.* 1993) would explain the existence of a thin crustal section. However, Grevemeyer *et al.* (2021) postulate that the shallowing bathymetry often observed in the transition between transform and fracture zone, results from crustal thickening caused by magma 'leakage' from the adjacent spreading centre through faults and fractures.

In this paper, we present the results of a multidisciplinary geophysical investigation of an ocean–continent transform margin that is currently actively evolving. Here, we focus on the ridge segment-transform-continental margin intersection.

2 STUDY LOCATION AND GEOLOGICAL SETTING

The Swan Islands transform margin is actively evolving (Mercier de Lepinay *et al.* 2016). Located in the Caribbean Sea at the southern edge of the Cayman Trough (Fig. 1), it is marked by the Swan Islands Transform Fault (SITF) and is one of few identified to be in Stage 2 of an evolution from initiation to abandonment as a fracture zone. Gravity and magnetic data (ten Brink *et al.* 2002) suggest that 2–3-km-thick oceanic crust, formed at the adjacent ultraslow spreading Mid-Cayman Spreading Centre (MCSC—full rate of 15–17 mm yr^{-1}—Holcombe & Sharman 1973; Dick *et al.* 2003; DeMets *et al.* 2007), is juxtaposed against 20–30-km-thick continental crust,

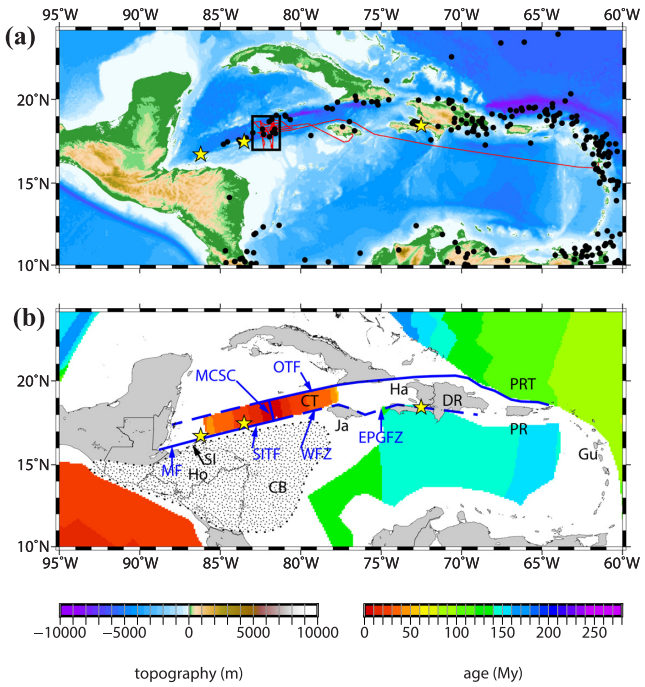

Figure 1. *CAYSEIS* project in the Cayman Trough. (a) Port-to-port ship track (red line). Black dots show earthquake locations, with the yellow stars marking the 2009, 2010 and 2018 $M_w > 7$ events (USGS Earthquake Hazards Program catalogue; https://earthquake.usgs.gov). Study area is outlined by the black box. (b) Oceanic crustal age (after Müller *et al.* 2008) in the Cayman Trough (CT), with the Caribbean-North America Plate boundary marked (blue line). Structural features: EPGFZ—Enriquillo-Plantain Garden fault zone; MF—Motagua fault; MCSC—Mid-Cayman Spreading Centre; OTF—Oriente transform fault; WFZ—Walton fracture zone. Geographic features: CB—Chortis Block; DR—Dominican Republic; Gu—Guadeloupe; Ha—Haiti; Ho—Honduras; Ja—Jamaica; PR—Puerto Rico; PRT—Puerto Rico Trench; SI Swan Islands. Chortis Block is dotted (after Rogers *et al.* 2007).

making this an ideal location to study how these margins evolve. The origin and evolution of the Swan Islands transform fault (SITF) boundary and the evolution of the Cayman Trough are described in Peirce *et al*. (2019b), with the accretion and evolution of the oceanic crust formed at the MCSC described in Harding *et al.* (2017), Van Avendonk *et al.* (2017) and Grevemeyer *et al.* (2018a) and references cited therein.

The SITF is part of a large strike-slip system that includes the Motagua fault (Honduras) and the Enriquillo-Plantain Garden fault zone (Fig. 1a). Little is known about its crustal structure apart from that revealed by a seismic reflection profile that runs across the northern Honduras margin (Sanchez *et al.* 2016) and by a wide-angle seismic profile that runs MCSC-parallel through 10-Myr-old Cayman Trough crust and extends onto the continental margin (Peirce *et al*. 2019b). The latter study showed that the SITF has higher velocities at shallower depths than observed in the oceanic crust to the north. It also showed that, subseabed, it is a fault zone no wider than ~5–10 km, that is mirrored by a narrow, ~7500-m-deep depression in the seabed. At greater depth it is underlain by a ~20-km wide, higher density region (>3000 kg m^{-3}) that may reflect a broad zone of mantle metasomatism, hydration or melt-depletion.

The MCSC, lying at the centre of the Cayman Trough, is the deepest known seafloor spreading centre, with an axial depth of >6000 m in places. The full spreading rate is ultraslow (<20 mm

yr^{-1}) and spreading has been on-going for the past 45.6 Myr (Rosencrantz *et al.* 1988; Leroy *et al.* 2000). Oceanic core complexes (OCCs) exist along the axial flanks (Hayman *et al.* 2011), with the central one, Mt Dent, hosting the Von Damm hydrothermal vent field in an exhumed mafic crustal root (Connelly *et al.* 2012; Harding *et al.* 2017; Van Avendonk *et al.* 2017; Grevemeyer *et al.* 2018a). Observation of OCCs (Haughton *et al.* 2019) suggests the crust formed by phases of tectonically dominated (magma poor) and magmatically dominated (magma rich) seafloor spreading (e.g. Olive *et al.* 2010). Such crustal formation likely results in a highly laterally variable crustal structure and thickness (Searle 2012), with the crust observed to be as thin as ∼3 km in places (Ewing *et al.* 1960; White *et al.* 2001; ten Brink *et al.* 2002; Van Avendonk *et al.* 2017; Grevemeyer *et al.* 2018a). Consequently, along the Swan Islands system not only can a transform margin that is actively evolving be studied, but also one that is acting, in many respects, as a magma-starved ocean–continent transition. In turn, such magma-starved margins are associated with significant stretching of the continental crust (e.g. Lavier & Manatschal 2006).

3 DATA ACQUISITION

The *CAYSEIS* (*Crustal accretion and transform margin evolution at ultraslow spreading rates*) project acquired active-source seismic, gravity and swath bathymetry data along six profiles (called Profiles P01–P06) in the Cayman Trough (Fig. 2—FS Meteor cruise M115—Peirce 2015; Grevemeyer *et al.* 2016), together with passive seismic data surrounding the Mt Dent OCC (Grevemeyer *et al.* 2019). Here we describe the southern section of one of these profiles (Profile P01—henceforth referred to as P01S) which is located at the MCSC spreading axis (zero-age crust), and traverses the SITF at the ridge-transform intersection (RTI), and extends across the Swan Islands transform ocean–continental margin. The other profiles acquired along and across the MCSC are described by Harding *et al.* (2017—Profile P02), Van Avendonk *et al.* (2017—Profile P01, northern section), Grevemeyer *et al.* (2018a—Profiles P05 and P06) and Peirce *et al.* (2019b—Profile P04).

Along Profile P01S, wide-angle (WA) seismic data were acquired with 25 ocean-bottom seismographs (OBSs) and hydrophones (OBHs) spaced at ∼5 km intervals along a total profile length of ∼165 km (Fig. 2b). Each OBS had a three-component geophone and a hydrophone, while each OBH was fitted with a hydrophone only (see Acknowledgments section for instrument sources). Henceforth, we refer to both instrument types as OBSs for simplicity. Data were recorded at 4 ms (250 Hz) sampling rate. Shots were fired using an array of 12 Sercel G airguns towed at 7.5 m depth. The total array volume was 5440 in^3 (∼89 l), which was fired at 60 s intervals at an air pressure of 3000 psi (∼207 bar). This firing interval, at 4.5 kn surveying speed, resulted in a shot interval of ∼150 m. Water waves and first-arriving refracted phases (crustal Pg and mantle Pn) are consistently observed (Fig. 3). However, Moho reflections (PmP) and second-arriving *S*-waves (Sg) are sparsely observed and are too few in number to analyse with any confidence in modelling outcome.

Gravity data were acquired port-to-port (see Fig. 1a for the cruise track) using a LaCoste-Romberg/Micro-G air-sea gravimeter mounted on a gyro-stabilized platform, tied to absolute base stations in Montego Bay (Jamaica) and Pointe-a-Pitre (Guadeloupe), the cruise port calls. Data were reduced to the free-air anomaly (FAA) for modelling. Bathymetry data were acquired along profiles using a Kongsberg Simrad EM122 multibeam echo-sounder, calibrated with a sound velocity profile conducted in the survey area to full ocean depth.

4 WIDE-ANGLE DATA TRAVELTIME PICKING

Seabed depth and degree of sediment cover control the signal-to-noise ratio (SNR) and events recorded in each OBS data set. Prior to traveltime picking, phase types were identified as water wave direct arrivals (Ww), their sea-surface/seabed multiples and crust and mantle refracted arrivals (Pg and Pn), by analysis of the OBS data displayed at a range of reduction velocities. Example record sections for OBSs 001, 113 and 125 are shown in Fig. 3, chosen to represent the three different geological settings (Fig. 2b): oceanic crust (OBS 113), continental margin crust (OBS 125) and ridge-transform intersection crust (OBS 001).

4.1. Oceanic crust: OBS 113

OBS 113 (Figs 3a and b) is located on 0-Myr-old oceanic crust ∼25 km to the north of the SITF (Fig. 2b), and shows clear evidence of *P*-wave first arrivals for ∼30 km distance either side of the OBS. PmP reflections are not unequivocally observed on any OBS located to the north of the SITF, which suggests that the Moho here may not be a distinct interface at the wavelength of the seismic signal generated by the G airgun array. Crustal Pg arrivals are observed at the nearest shot-receiver offsets as there is little-to-no sediment cover, while Pn arrivals are generally observed at offsets >15 km from the instrument. Undulation in first-arrival traveltimes is largely a function of variation in seabed topography along profile.

4.2. Continental margin crust: OBS 125

OBS 125 (Figs 3c and d) is located on the continental slope towards the southern end of the profile (Fig. 2b). The shallowing seabed depth to the south of this instrument results in the observed record section asymmetry. Crust and mantle refracted arrivals are clearly observed, together with a set of slower apparent velocity arrivals adjacent to the instrument location. These arrivals could suggest a relatively thin veneer of sediment cover and may explain the better SNR of instruments to the south of the SITF, due to the better seabed sensor coupling and less signal scattering as a result. Pn arrivals are observed at shot-receiver offsets of >40 km. The only PmP arrivals unequivocally observed anywhere along Profile P01S are observed by instruments located to the south of the SITF and, even then, they are of low amplitude and sparse.

4.3. Ridge-transform intersection crust: OBS 001

OBS 001 (Figs 3e and f) is located at the intersection between the MCSC and the SITF, the deepest topographical point along the profile (Figs 2b and c). Pg arrivals can be observed from the shortest offsets which suggests that a significant thickness of sediment originating, for example, from the adjacent continental margin, has not accumulated within the SITF. Pn arrivals are evident at offsets >35 km to the north of the instrument.

First-arrival traveltimes were picked from the hydrophone records, as these displayed the highest SNR. A pick uncertainty of 75 ms was assigned for each subseabed travelling phase regardless of shot-receiver offset, calculated based on instrument and shot

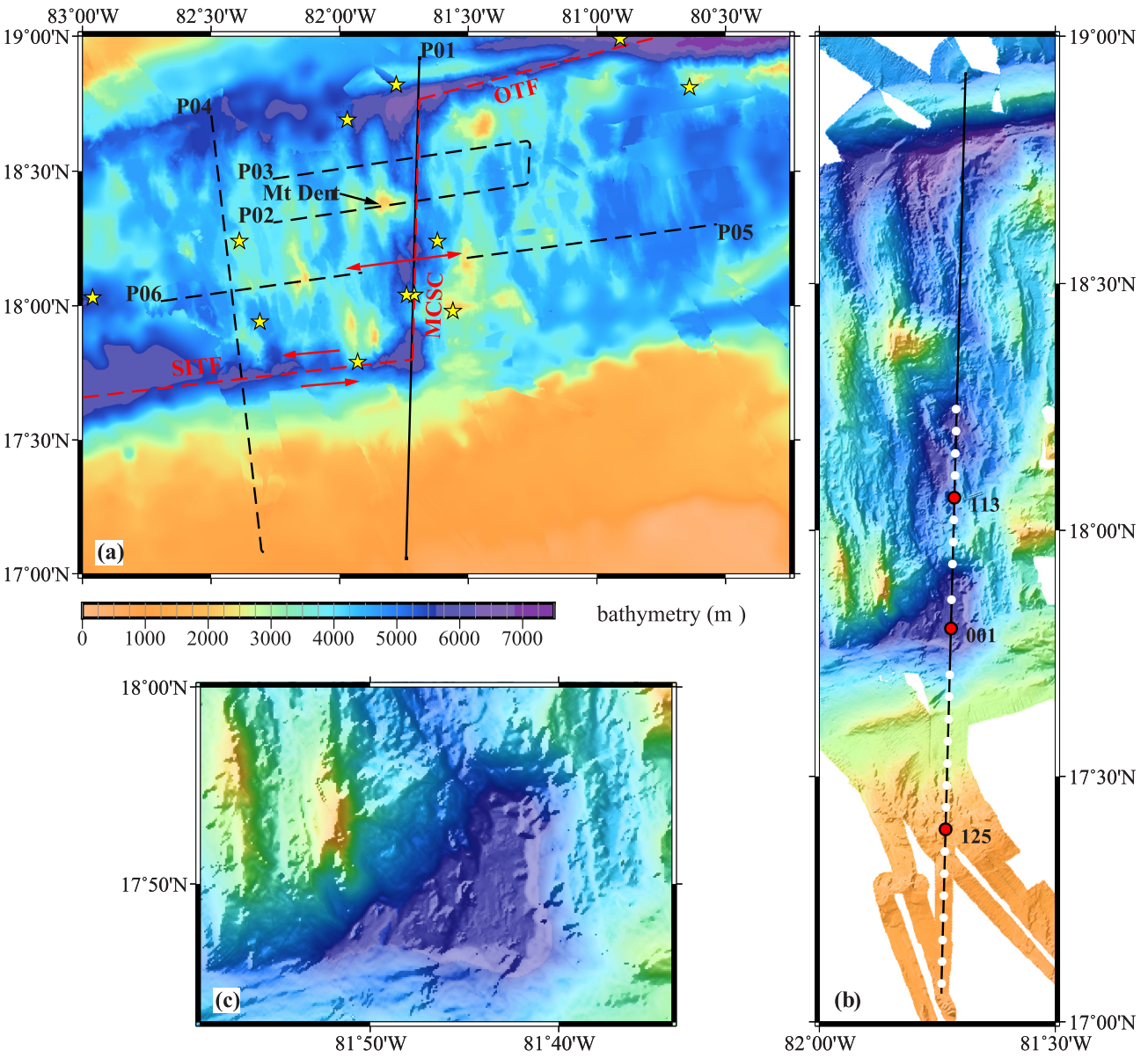

Figure 2. Cayman Trough and adjacent Honduran continental shelf and slope bathymetry. (a) Profiles from the *CAYSEIS* experiment are shown by black solid and dashed lines. Dashed red line shows the Swan Islands transform fault (SITF) to the south and the Oriente transform fault (OTF) to the north, with red arrows showing the left-lateral slip direction of the SITF and the spreading direction of the MCSC. The Mt Dent OCC is labelled and earthquake epicentres are marked by yellow stars. (b) Profile P01 with OBSs used in this study shown by white circles. The locations of OBSs 001, 113 and 125, whose recorded data is shown in Fig. 3, are highlighted in red. (c) High-resolution bathymetry showing the MCSC ridge-transform intersection.

location errors. Approximately 11 000 first-arrival traveltime picks were made from 25 receiver gathers.

5 WIDE-ANGLE DATA INVERSION MODELLING

Prior to inversion, OBS locations on the seabed were determined by forward ray trace modelling water wave arrivals (Ww) and their multiples using *rayinvr* (Zelt & Ellis 1988; Zelt & Smith 1992). The water column velocity structure used to calibrate the swath bathymetry acquisition system was used for this modelling. The model seabed interface was created by sampling the bathymetry at 0.25 km intervals along-profile (Fig. 2b), and projecting these and the OBS and shot locations into kilometre-space relative to 17°03.445′N/81°44.480′W—the most southerly shot point—prior to padding the model at either end to minimize edge effects. The inversion forward model was discretized on a 0.25 by 0.25 km uniform square mesh (the forward cell size), which was kept constant throughout modelling.

5.1. Inversion process

Pg and Pn arrival traveltime picks were inverted for *P*-wave crustal velocity–depth structure using the *FAST* inversion method of Zelt & Barton (1998), as it is a modeller-independent process that can also be used to test the resolution of the resulting velocity–depth model (Zelt *et al.* 2003). Initially, the starting model was

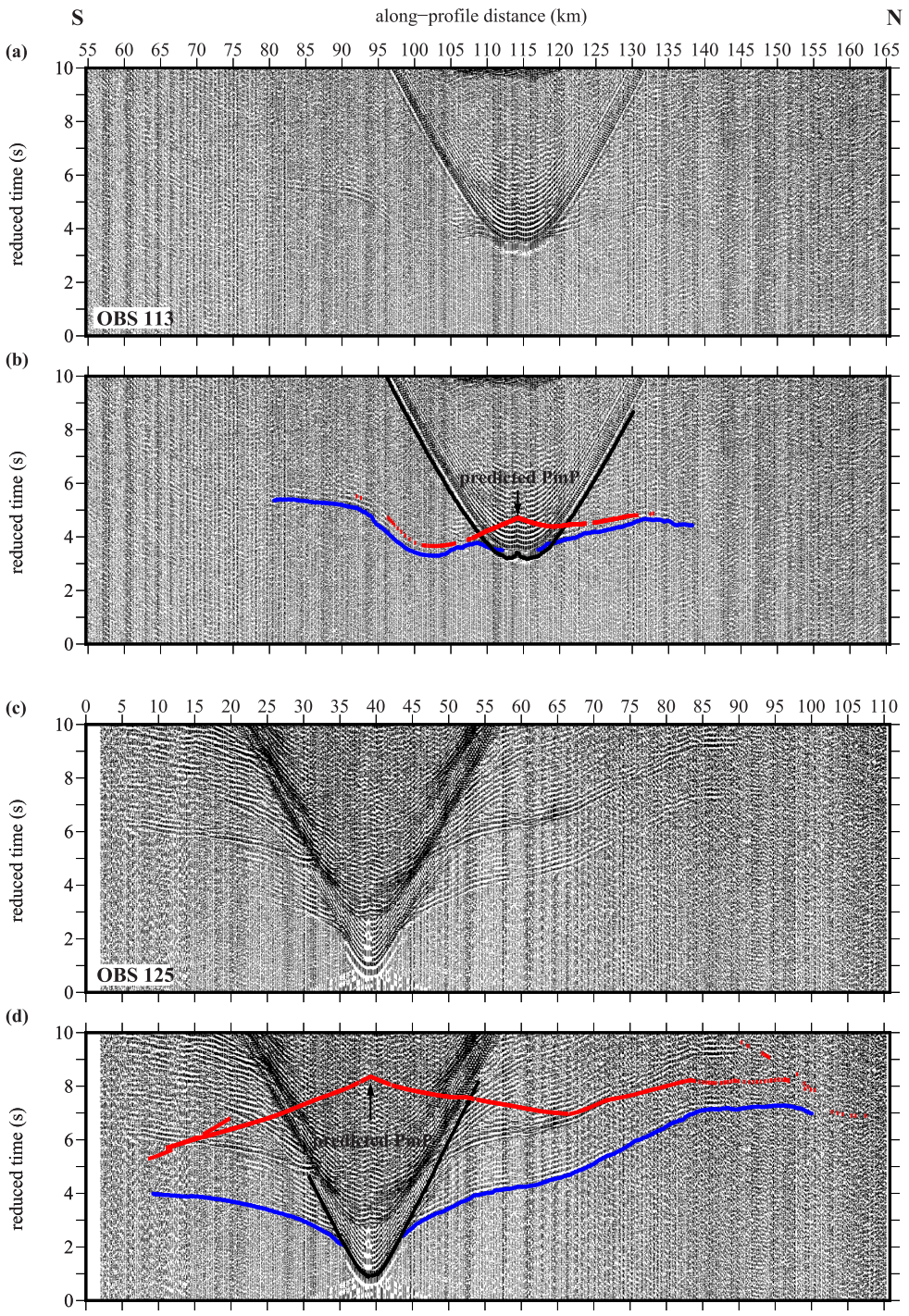

Figure 3. Example hydrophone WA refraction data sections (see Fig. 2 for location). (a) Record section for OBS 113 (oceanic crust) plotted with a reduction velocity of 8 km s^{-1} and a 1–2-20–30 Hz bandpass filter. Horizontal axis shows along-profile distance (*cf.* all model figures). (b) Record section showing observed water wave (Ww—black) and crust and mantle *P*-wave (Pg and Pn—blue) arrival traveltime picks. Phases are labelled and traveltime pick symbol size shows corresponding uncertainties. Predicted Moho reflection (PmP) based on forward modelling (Fig. 9) is also shown (red). (c and d) Record sections for OBS 125 (continental margin crust). (e and f) Record sections for OBS 001 (ridge-transform intersection crust). *Note*: PmP reflections are sparse and only observed on a number of OBSs to the south of the SITF.

constructed by applying beneath a seabed interface a 1-D velocity model, comprising a velocity of 2.0 km s^{-1} at the seafloor and 8.5 km s^{-1} at a fixed depth of 15 km below sea level (b.s.l.) to represent a constant depth Moho starting point (Fig. 4a), approximately mid-way between that of average oceanic and continental crusts. This starting model—the *fixed bottom initial model*—enabled the greatest modelling freedom within existing geological constraint but, more importantly, did not impose any structure or velocity–depth expectation for any crustal type along profile (e.g. the change of gradient that might be expected within the oceanic crust reflecting the transition from the basalts of layer 2 to the gabbros of layer 3).

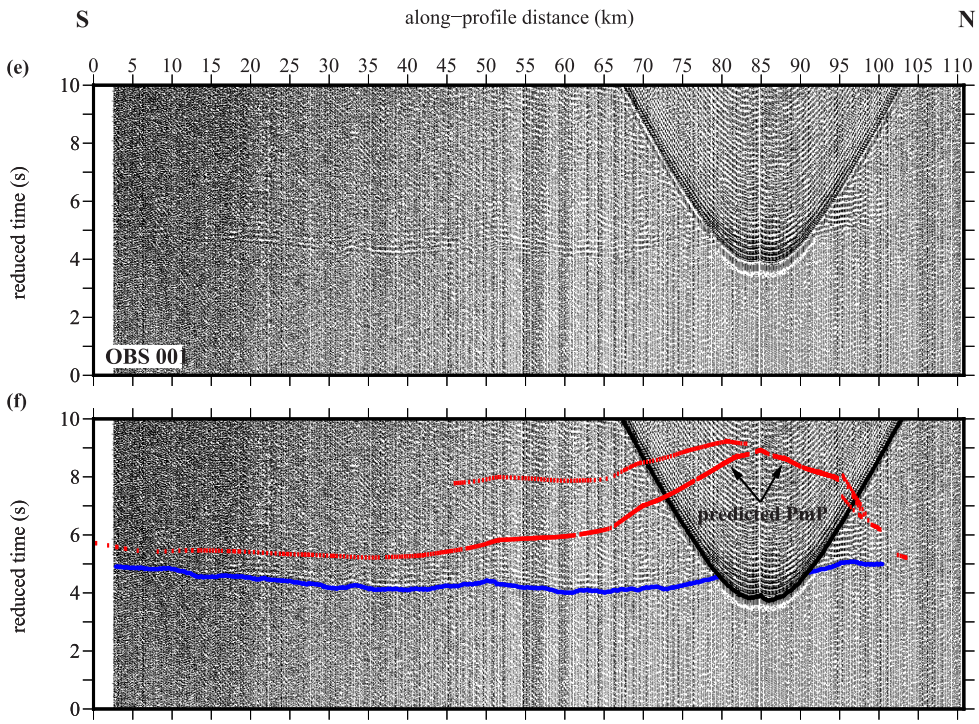

Figure 3. Continued.

The inversion was run in three phases, each of four non-linear inversion iterations, with the inversion cell size reduced between phases from 2.0 × 2.0 km for phase 1, 1.0 × 1.0 km for phase 2 and 0.5 × 0.5 km for phase 3. The model resulting from each phase was used as the starting model for the next. As Fig. 5 shows, after phase 1 the velocity–depth model did not change significantly between successive phases, with a root-mean-square traveltime (T_{RMS}) misfit of ∼159 ms and a $\chi^2 = \sim 4.5$ after phase 1, improving to a T_{RMS} misfit of ∼123 ms and $\chi^2 = \sim 2.7$ after phrase 2, and ∼106 ms and $\chi^2 = \sim 2.0$ for the final model (henceforth the *P-wave inversion model*). The inversion parameters are summarized in Table 1 and Fig. 5 shows the results of the inversion. It is good practice to pad an inversion model beyond the extent of the ray coverage to avoid incorporation of edge effects. Consequently, the edges of the final model will remain quite similar to that of the initial model, since the structure and velocity–depth characteristics are not constrained by any traveltime picks. Thus, areas of the models not constrained by ray coverage are masked out in the figures for clarity.

Velocity anomalies are observed within the oceanic crustal part (∼100–140 km along-profile distance) of the final model which could be modelling artefacts either stemming from individual OBS positions (sets of traveltimes), their pattern of ray coverage or the characteristics of the initial starting model. The crustal thickness and velocity–depth profile beneath the margin also appears to be controlled by a partitioning between two sets of arrivals from two adjacent model domains. To test the dependence of the final model on the starting point, two other styles of starting model were tested:

(i) A pseudo-1-D constant thickness crust that follows the seabed—the *seabed following initial model* (Fig. 4b).

(ii) A 2-D model in which crustal thickness increases from north to south along profile, to accommodate the likely crustal thickness difference between continental and oceanic domains—the *sloping bottom initial model* (Fig. 4c).

The results of inversion based on these starting models can be found in Figs Supplement 1 and 2, with the *seabed following initial model* resulting in a T_{RMS} misfit of ∼109 ms and $\chi^2 = \sim 2.1$, and the *sloping bottom initial model* resulting in a T_{RMS} misfit of ∼107 ms and $\chi^2 = \sim 2.0$; essentially equivalent statistically and with features consistent with the *P-wave inversion model*, including the apparent significant crustal thinning that occurs adjacent to the ridge-transform intersection (*ca.* 100 km along-profile distance). In all models, this location corresponds with a low ray coverage density (*cf.* Figs 5d, Supplement 1d and Supplement 2d) which is largely due to the limited extent (<∼20 km to north and south of OBS only) of arrivals recorded by OBS 115 and 116 deployed at the southernmost end of the MCSC.

5.2. Model resolution testing

Checkerboard tests were performed to appraise the resolution of the *P-wave inversion model* (Fig. 6) and determine the smallest structures resolvable by the acquisition geometry and model parametrization (Zelt 1998). We adopted this approach to be consistent with that adopted for Profile P04 (Peirce *et al.* 2019b), so that the modelling outcomes are directly comparable. As such, a regular checkerboard of alternating polarity 5 per cent velocity perturbations was convolved with the *P-wave inversion model*, which was then ray-traced to create synthetic traveltimes for each OBS location. Gaussian noise was then added based on the pick uncertainty. These synthetic traveltimes were inverted using the same parameters used to derive the *P-wave inversion model*, with the process repeated for a broad range of checkerboard cell sizes and patterns. These patterns included vertical and lateral shifts of patterns aligned vertically (columns) and horizontally (rows), inverting the polarity of the checkerboard velocity (positive and negative), half shifts in cells (across rows and down columns) and all possible combinations thereof—14 unique patterns in total. To assess

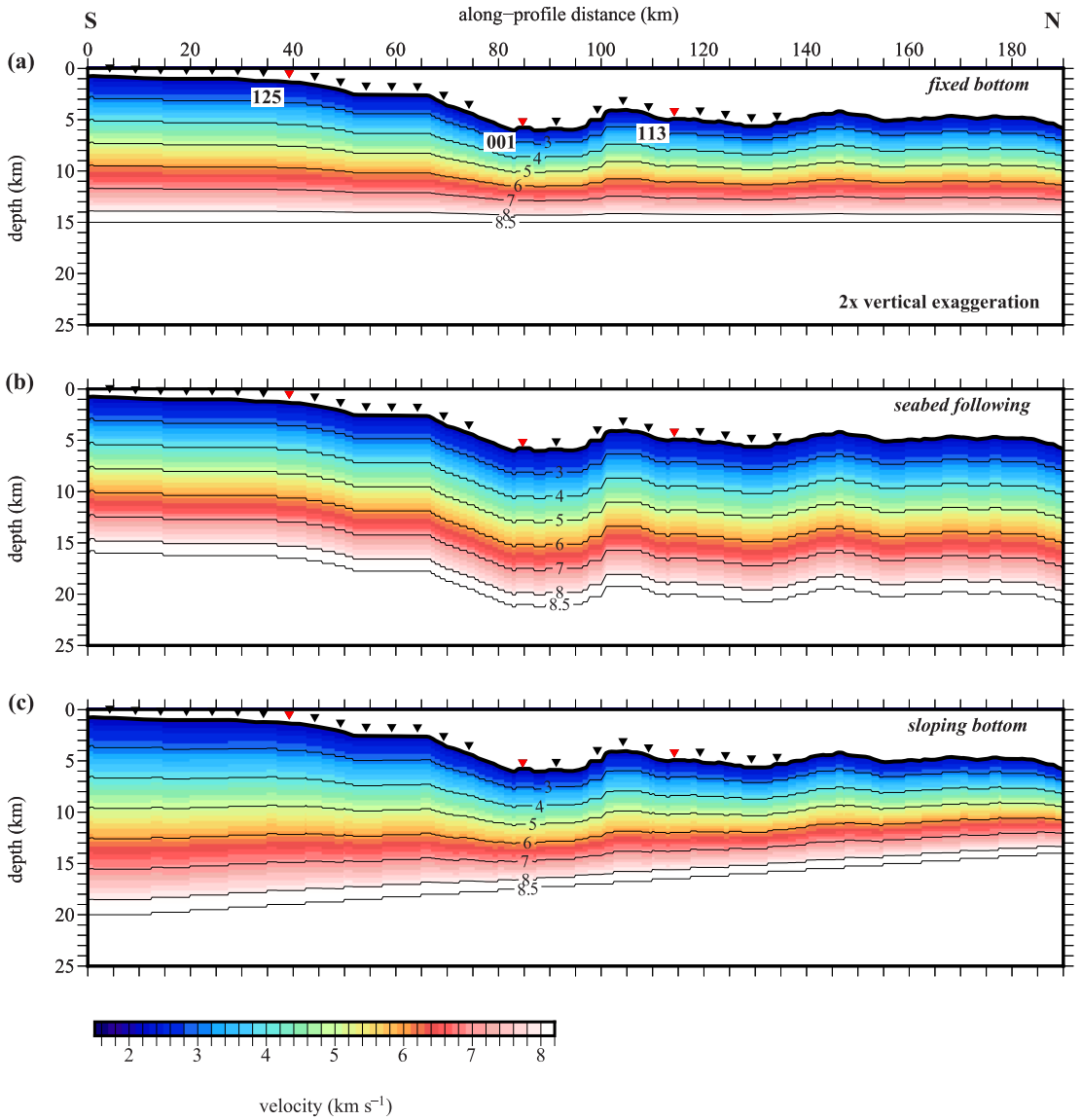

Figure 4. Inversion modelling initial models. (a) *Fixed bottom initial model*. The inversion outcome using this starting model is shown in Fig. 5. (b) *Seabed following initial model*. The inversion outcome using this starting model is shown in Fig. S1. (c) *Sloping bottom initial model*. The inversion outcome using this starting model is shown in Fig. S2. OBS locations are shown by inverted black triangles, with OBSs 001, 113 and 125, whose recorded data is shown in Fig. 3, shown by red inverted triangles.

the checkerboard tests quantitatively, the correlation between the applied and recovered checkerboards was calculated for each of the tested patterns. Zelt (1998) refers to this correlation as semblance, and defines a threshold value of 0.7 as showing where a model is well-resolved. The semblance calculations show that the lower continental slope and southern end of the MSCS are well-resolved to the scale of anomaly variation necessary to determine crustal structure and any lateral variation within it (5 km laterally by 2 km vertically), the ridge-transform intersection crust less so.

In general terms, for an applied ±5 per cent velocity anomaly, structures in the crust at the southern MCSC ridge tip are consistently constrained with confidence to 5-km wide by 2-km deep to a depth of ∼5 km below seabed (b.s.b.) (Fig. 6f), and for the upper-to-mid continental margin crust to a depth of ∼10 km b.s.b. (Fig. 6f) and 10 km-wide by 4-km deep for the upper crust beneath the ridge-transform intersection to a depth of ∼4 km b.s.b. (Fig. 6i).

5.3. Consistency with other *CAYSEIS* models

Fig. 7 shows a comparison between the *P-wave inversion model* (P01S) and the other profiles acquired as part of the *CAYSEIS* project and analysed to date, highlighting in particular the points of intersection. It should be noted that the *CAYSEIS* profiles were independently modelled, using different approaches to inversion and to starting model creation. Inevitably, this may lead to apparent differences between final models at the intersection points, especially so in parts of the models where there is sparse or no ray coverage constraint, such as within the lower crust and uppermost mantle.

The northern section of P01 (P01N on Fig. 7c) was analysed by Van Avendonk *et al.* (2017), focusing on the accretionary processes occurring at the MCSC. The northern and southern sections overlap by ∼40 km to provide ray coverage to the base of crust/uppermost mantle in both for modelling purposes. These independently derived models are remarkably consistent given the contrasting

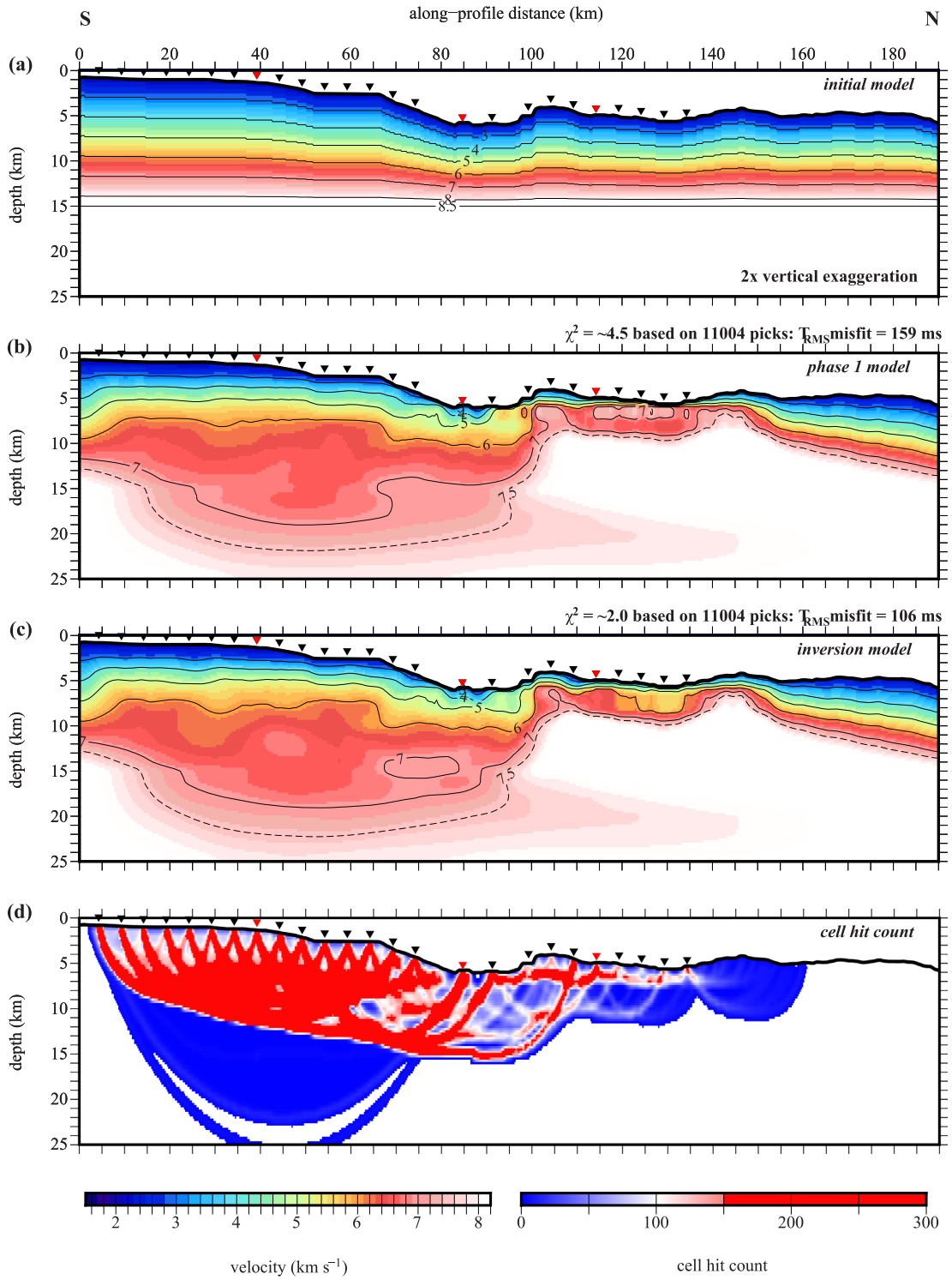

Figure 5. Inversion modelling. (a) *P-wave initial model*. (b) *Phase 1 interim model*. (c) Best-fitting *P-wave inversion model*. See text and Table 1 for approach and parameters adopted. χ^2 fit, the root-mean-square misfit (T_{RMS}) and the number of traveltime picks are labelled for each stage. Velocity contours are plotted at 1.0 km s^{-1} intervals, together with the 7.5 km s^{-1} contour used as a proxy for base of crust. (d) Cell hit count indicatively showing ray coverage used to mask the *P-wave inversion model* in other figures. In all parts, OBS locations are marked by inverted black triangles, with OBSs 001, 113 and 125 highlighted in red.

inversion approaches adopted. Modelling suggests that the MCSC crust is consistently 3–4-km-thick along axis, even at the ridge tip adjacent to the SITF. Profile P01 traverses three other across-axis profiles (Figs 2 and 7a). Profiles P05 (east of MCSC axis) and P06 (west) together form a transect crossing the MCSC running along a flow-line approximately mid-segment (Fig. 7d—Grevemeyer *et al.* 2018a). Profile P02 (Fig. 7e—Harding *et al.* 2017) runs across-axis in the vicinity of the Mt Dent OCC. Again, these models are remarkably consistent where they intersect with the *P-wave inversion model*, with the former showing how laterally variable the crust is

Table 1. Summary of *P*-wave inversion parameters (after Zelt & Barton 1998).

Inversion parameter		*P*-wave model
sz		0.225
alpha		0.95
lambda0		1000
lambda reduction factor		1.414
Inversion cell—first phase	Horizontal	2.0 km
	Vertical	2.0 km
Inversion cell—second phase	Horizontal	1.0 km
	Vertical	1.0 km
Inversion cell—third phase	Horizontal	0.5 km
	Vertical	0.5 km

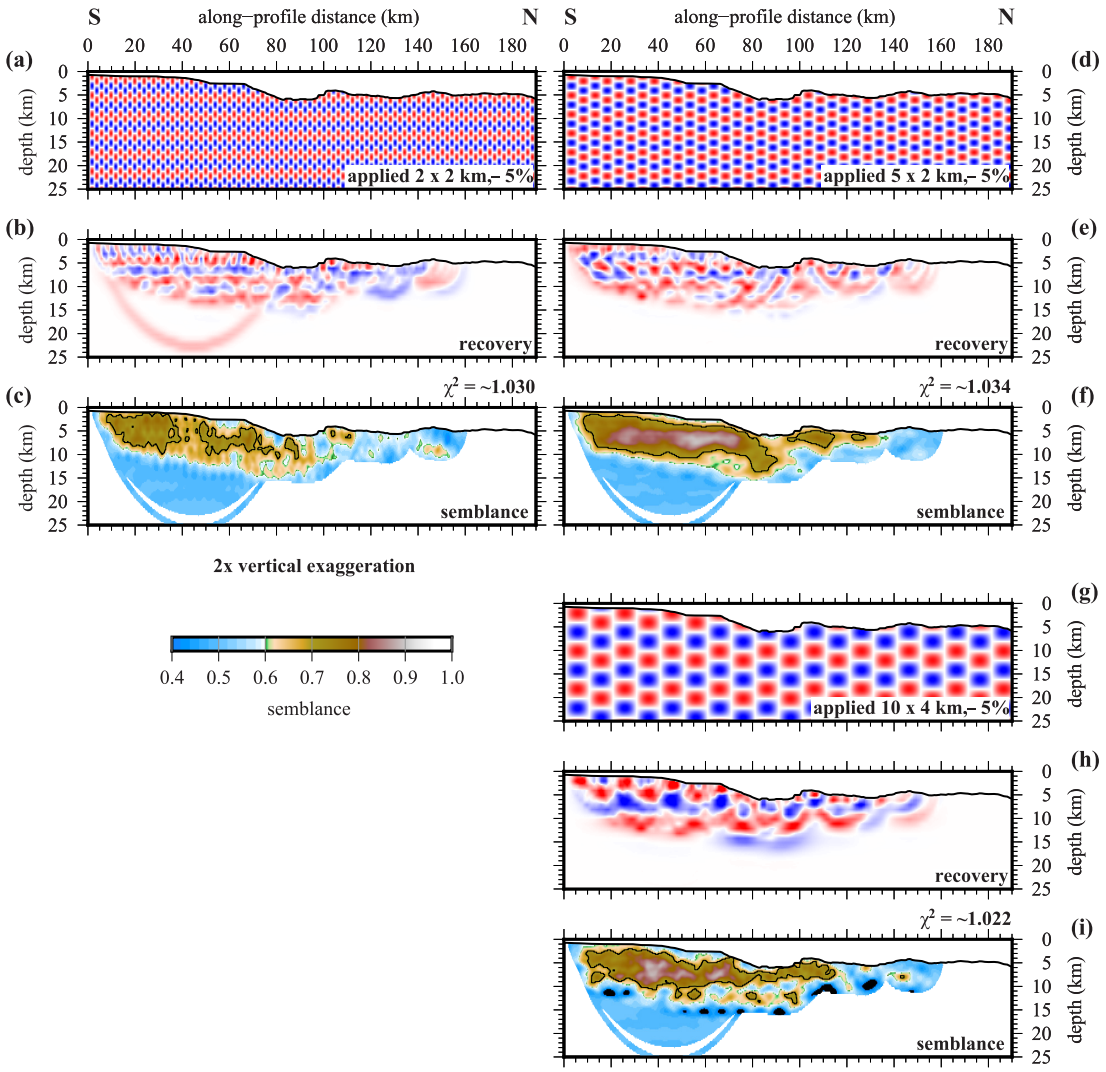

Figure 6. Checkerboard resolution testing of the *P-wave inversion model*. (a) Checkerboard applied to the *P-wave inversion model* with a 2 × 2 km pattern size and 5 per cent velocity anomaly. (b) Recovered checkerboard. (c) Semblance masked by ray coverage. A semblance of 0.7 is used as the good resolution threshold. χ^2 fit is annotated. A good resolution is achieved for the top ~5–7 km of the continental crust. (d–f) Checkerboard testing with a 5 × 2 km and 5 per cent velocity anomaly checkerboard. A good resolution is achieved to ~10 km depth in the continental crust and beneath the SITF, and to ~3–5 km beneath the MCSC. (g–i) Checkerboard testing with a 10 × 4 km and 5 per cent velocity anomaly checkerboard.

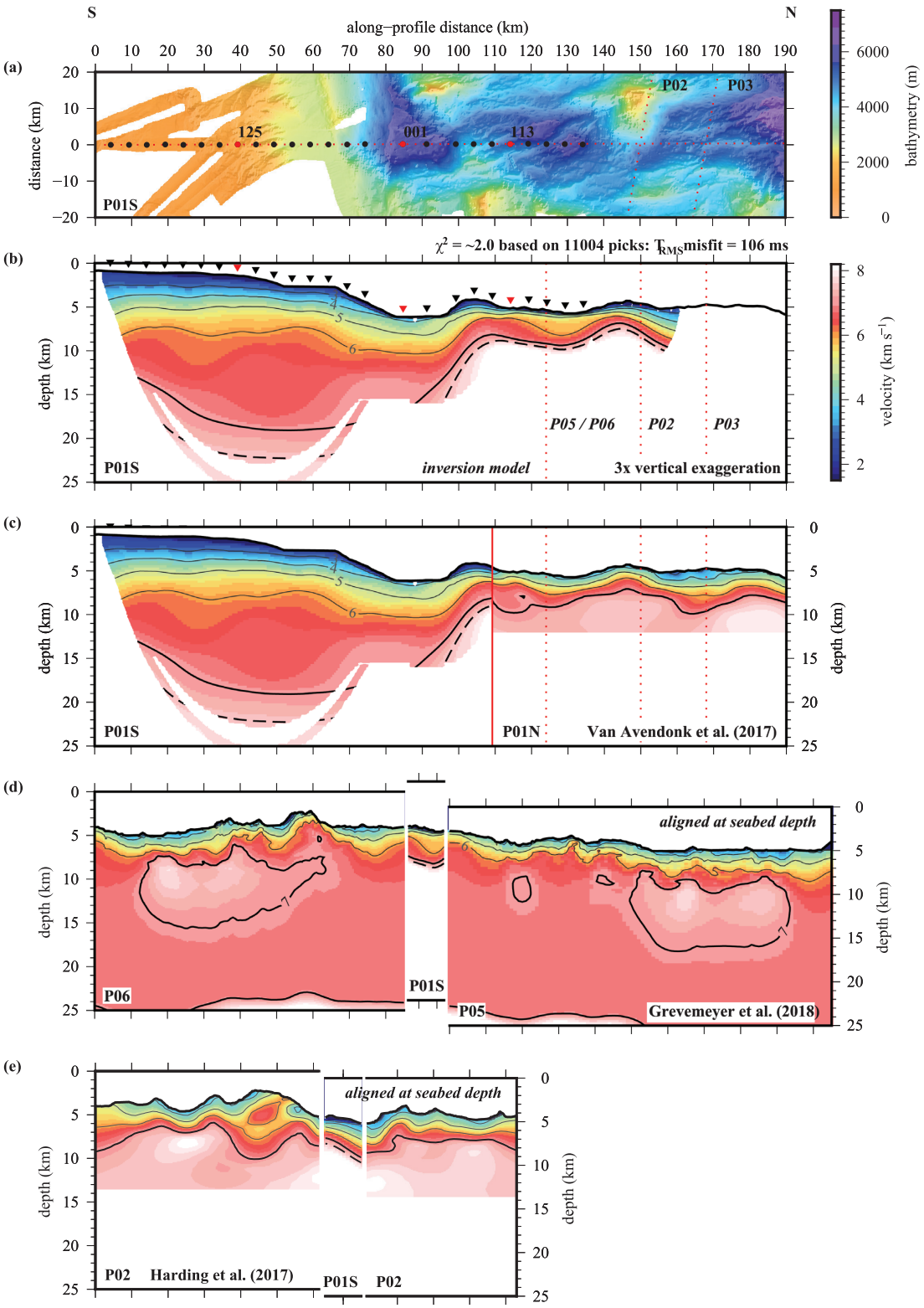

Figure 7. Comparison between *CAYSEIS P-wave inversion models*. (a) Swath bathymetry surrounding Profile P01S. OBS locations (black dots/inverted triangles) shown in all parts, with OBSs 001, 113 and 125 (red dots/inverted triangles) highlighted. Profiles P01, P05 and P06 (extrapolated) and P02 and P03 (intersecting along the northern end of Profile P01 as a whole) are marked by red dotted lines. (b) *P-wave inversion model* for Profile P01S. (c) Comparison between the inversion model of this study for the southern section of Profile P01 (P01S) and that of Van Avendonk *et al.* (2017) for the northern section (P01N), showing a very good correlation, despite different approaches to inversion being adopted, over the ~40 km overlap. (d) Comparison between *P*-wave velocity–depth models for Profiles P06 and P05 (Grevemeyer *et al.* 2018a) and Profile P01S at the MCSC. (e) Comparison between the *P*-wave velocity–depth models for Profile P02 (Harding *et al.* 2017) and P01S at their intersection. In parts (b–e) velocity contours are plotted at 1.0 km s^{-1} intervals (thin black lines), with the 7.0 km s^{-1} contour shown by a thick black line. The 7.5 km s^{-1} contour (black dashed line) is used as a proxy to define the Moho.

within the Cayman Trough, and together they provide a 3-D perspective on spreading evolution at the MCSC. Of particular note here is the degree of crustal thickness variation demonstrated by Profiles P05 and P06 (Fig. 7d), which is attributed to a waxing and waning magma supply at the ridge axis that, in turn, causes a transition between magma poor, tectonically dominated spreading and magma rich crustal accretion. In this context, the consistency in crustal thickness observed along the MCSC to the ridge-transform intersection, and the lack of higher velocity anomalies at or in the vicinity of the seabed, suggest that the ultraslow-spreading MCSC, from mid-segment to southern spreading ridge tip, may currently be in a magma rich phase.

6 MODEL CONSTRAINTS

The free-air gravity anomaly (FAA—Fig. 8c) provides an independent test of velocity–depth structure and can be used to constrain poorly resolved regions. Therefore, the *P-wave inversion model* was converted into a density model (Fig. 8a—henceforth the *constant density model*) consisting of 2-D polygons with upper and lower boundaries based on the 4.0, 5.0 and 6.0 km s^{-1} velocity contours (*cf.* traditional oceanic crustal layering—White *et al.* 1992) and using the 7.5 km s^{-1} contour as a proxy for the base of the crust based on the conclusion drawn by Peirce *et al.* (2019b) that, at the MCSC, the Moho is a transition zone. The model was extended 1000 km laterally to negate edge effects during anomaly calculation.

6.1. Initial modelling

The Carlson & Raskin (1984) velocity–density relationship for the oceanic crust was used to construct the initial *constant density model* (Fig. 8a), with densities of 2600, 2700, 2900 and 2950 kg m^{-3} applied for the individual crustal layers, 1030 kg m^{-3} assigned to the water column, and 3330 kg m^{-3} for the mantle. The FAA (Fig. 8c) was calculated using *grav2d*, modified from the original programme written by J.H Luetgert and based on the Talwani *et al.* (1959) algorithm.

Comparison with the observed shows that, although mirroring the general along-profile wavelength variation in the FAA, a significant regional mismatch is observed, with the calculated FAA being too high to the south and north of the SITF, and too low at the SITF itself (Fig. 8c). Consequently, the *constant density model* was subdivided into a series of seven lateral zones within which the density could be independently adjusted within each layer of each zone. Modelling then aimed to determine the density–depth structure required to achieve the best fit to the observed anomaly to within ±5 mGal error—the cross-over error between all *CAYSEIS* gravity profiles.

6.2. Gravity fit

As a starting point for lateral and vertical density variation assignment along-profile, to the north of the SITF the velocity–density relationship of Carlson & Raskin (1984) was applied. This model was chosen so that no preconceived idea of the velocity–density–depth structure was imposed, other than that of oceanic crust. For the continental crust, in regions where the velocity is greater than 6 km s^{-1}, the relationship of Christensen & Mooney (1995) was applied, whilst considering the implications of the Carlson & Miller (2003) relationship for serpentinized mantle as applied in Prada *et al.* (2014). The Christensen & Mooney (1995) relationship is not applicable for velocities less than 6 km s^{-1}, so the relationship of Ludwig *et al.* (1970) was used instead. The densities assigned to each of the blocks for modelling, including incorporating a lateral density gradient within the mantle to match the longer wavelength component, are summarized in Table 2.

Although now a good fit along the majority of the profile, the calculated anomaly (Fig. 8c) still mismatches around the SITF. Consequently, further blocks were added vertically beneath the seabed (Fig. 8b) until a fit to the observed FAA was achieved (Figs 8c and d). To achieve this best fit (henceforth the *density model*) blocks with densities of 2800, 3150 and 3320 kg m^{-3} were required.

6.3. Inversion comparison

The *density model* was used to appraise areas poorly constrained within the *P-wave inversion model*, primarily due to a lack of deep crustal ray coverage (e.g. beneath the continental margin). These areas are identified by the mismatch between the base of the lower crustal blocks and the 7.5 km s^{-1} contour as shown in Fig. 8b. Gravity modelling suggests a more rapid thinning of the crust beneath the margin. In comparison to further along the margin (∼10 Ma—Peirce *et al.* 2019b) where modelling suggests that the continental crust appears to have undergone two stages of thinning (along-profile distance 40–60 km), in this more proximal area the best-fitting *density model* suggests thinning has been effectively consistent during margin evolution.

Perhaps the most notable difference between the crustal structure implied by the *P-wave inversion model* and that from the *density model*, is the variation in crustal thickness south of the ridge tip (*ca.* P01 along-profile distance 80–100 km), even where constrained by ray coverage. This is particularly notable beneath the SITF, where gravity modelling suggests a crust approximately a third as thick as the seismic inversion, and beneath the continental slope where gravity modelling suggests a crust about one third thinner than that derived from inversion. To the north of the ridge tip, the gravity modelled crustal structure is consistent with the seismic equivalent in terms of layer thickness, although the gravity modelling suggests lower densities (by 200–300 kg m^{-3}) than the seismic velocities imply, although not dissimilar to the expected modelling error in density terms.

As the *density model* is also generally consistent with that along Profile P04 (Peirce *et al.* 2019b), it is considered to be a valid, although smoothed, representation of the true structure of the entire crust and upper mantle. However, based on the gravity modelling the *P-wave inversion model* is only considered valid for the shallow-to-mid crust along the entire profile, and for the entire crust and upper mantle to the north of the SITF, in areas with more than 100 cell hits as part of inversion modelling (*cf.* Fig. 8b with Figs 5 and 6).

6.4. Ray-trace check

As a further means to test which of the *P-wave inversion* and *density models* is a more likely representation of the true crustal structure beneath the active transform margin and SITF/ridge-transform intersection, the *P-wave inversion model* was converted into a node-specified model with distinct layer boundaries imposed (Fig. 9a). The model (henceforth the *forward seismic model*) retains the lateral velocity anomalies in the upper crust, a thinned continental crust and a sharp lateral velocity transition associated with the SITF, and modelling was undertaken without adjusting any layer velocity or ascribed interface depth.

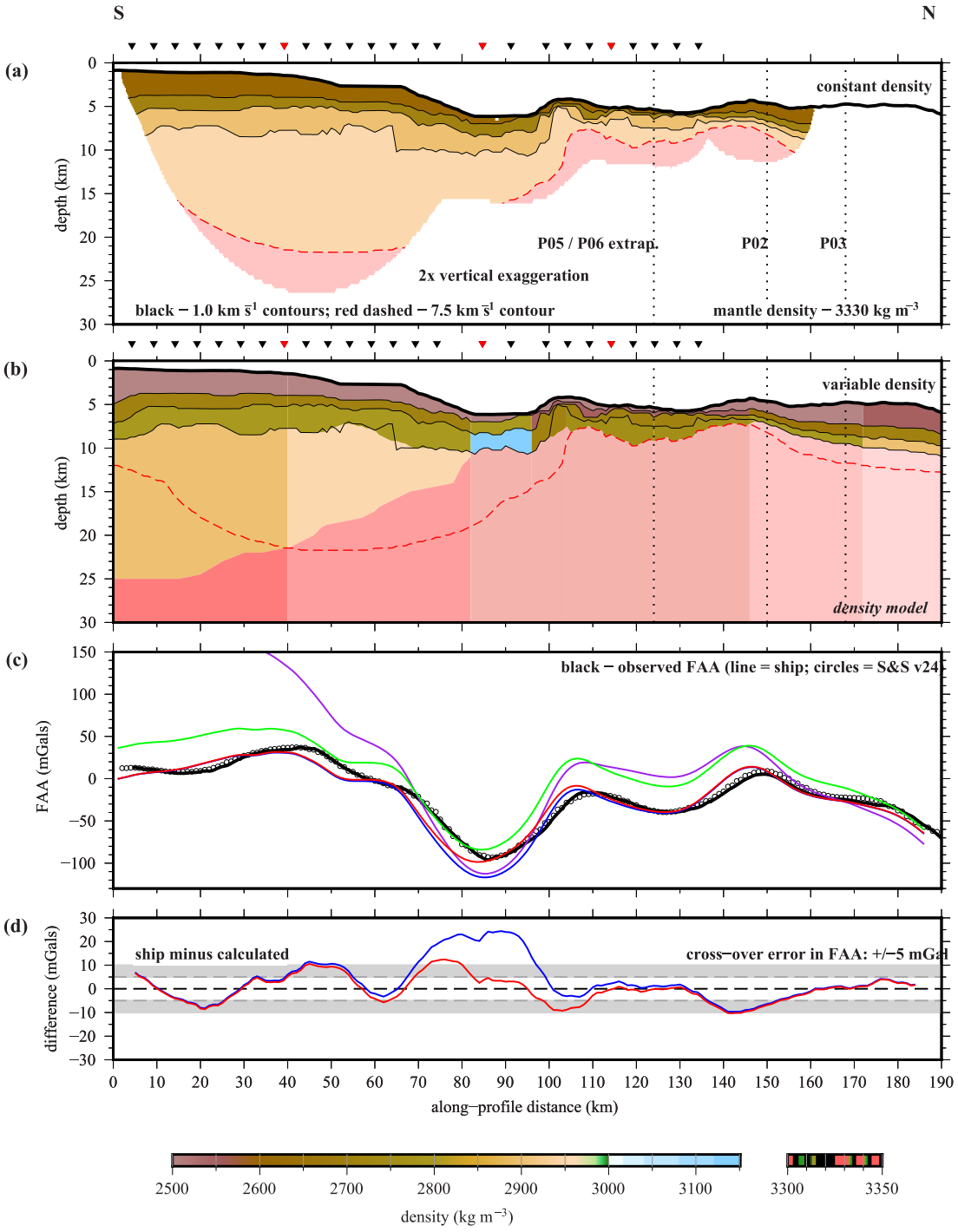

Figure 8. Gravity modelling test of the *P-wave inversion model*. (a) Density–depth model with solid black lines marking the 4.0, 5.0 and 6.0 km s^{-1} velocity contours, and the red dashed line the 7.5 km s^{-1} velocity contour used as block boundaries initially. Constant densities were applied to blocks within the same layer. Dotted vertical lines mark Profiles P05/P06, P02 and P03 (left to right) intersections. OBS locations are marked by inverted black triangles, with OBSs 001, 113 and 125 highlighted in red. (b) *Density model* with variable densities within each layer, together with a gradation in density within the mantle, required to achieve the best fit to the observed free-air anomaly (FAA). At the SITF (82 to 96 km along-profile distance) higher densities are required in the lower crust/upper mantle. See text for discussion and interpretation. (c) Observed (ship—black line; Sandwell & Smith 2009 v24–open circles) and calculated (coloured lines) FAAs, showing that higher density crust at the SITF is required to achieve a fit. Coloured lines represent anomalies calculated on the basis of: constant density blocks within layers with blocks defined solely by velocity contours (purple); constant density blocks within layers with blocks adjusted to achieve a longer wavelength fit (green); variable density blocks within layers consistent with their continental or oceanic location (blue); and variable density blocks including a higher density region beneath the SITF (red) required to achieve the best fit. (d) Misfit of the variable block density models plotted against FAA error bound.

Table 2. Summary of *density model* block densities.

Crustal region	Density (kg m^{-3})
Continental crust	
Upper	2600–2700
Lower	2800–2950
Mantle	3310–3315
Oceanic crust	
Upper	2500–2700
Lower	2700–2950
Mantle	3320–3325
SITF	
Upper	2500–2800
Lower	3150
Mantle	3320

The observed first-arrival traveltime picks were forward point-to-point ray-traced using *rayinvr* (Zelt & Ellis 1988; Zelt & Smith 1992—Fig. 9b), first by assuming that they are all Pg arrivals, and then assuming that they are all Pn arrivals as an additional test of the original phase identification. The results for OBSs 001, 113 and 125 are shown in Fig. 9(b) (ray diagram) and Figs 9(c)–(e) (traveltime pick fits). Consequently, the resulting misfit should be regarded as a proxy only for which of the inversion or gravity models is more likely a true reflection of actual crustal structure, and not as the forward ray tracing best fit that might be achieved if layer velocities and interfaces were further adjusted. The modelling shows that at the SITF and along the southern end of the ridge-axis calculated arrivals are consistently too slow, which implies that the velocity recovered in the *P-wave inversion model* is too low, particularly at depth.

The crustal thickness mismatch between the *P-wave inversion* and *density models* between 0 and 100 km model distance was further appraised by forward predictive ray tracing of potential PmP arrivals through the model, by tracing all possible PmP ray paths and comparing their arrival times with the sparely observed arrivals. Examples are shown in Fig. 9 for OBSs 113 (sited on 0-Myr-old oceanic crust ∼25 km to the north of the SITF), 125 (sited on the continental slope) and 001 (sited at the ridge-transform intersection), with the calculated phases also compared to the observed data in Figs 3(b), (d) and (e), respectively. This modelling shows that, if the base of the crust where a distinct interface and not a transition into the mantle, PmP arrivals would be observed either arriving within the high amplitude water wave, or mostly coincident with the first arrival multiple. The implication of this result is that either the Moho is a transition zone, or that the velocity contrast across the Moho is small, thus generating a PmP arrival amplitude indistinguishable above that of the background noise or earlier arriving phases.

7 RIDGE-TRANSFORM INTERSECTION

Both the gravity and forward ray tracing approaches suggest that the inversion may be sitting in a local minimum, with the structure determined within the SITF representing a fit, but not necessarily the best or only fit within the errors. To test this possibility an inversion starting model was created that was seeded with the SITF crustal structure implied by the gravity modelling (Fig. 10a) imposed on the *sloping bottom initial model* (Fig. 4c) to also test what influence the background representation of the crust might have. This inversion shows that such a model also results in a similar fit to the errors (T_{RMS} misfit of ∼107 ms and χ^2 = ∼2.0). Statistically, the *P-wave inversion* and *seeded inversion models* are equivalent, but suggest quite contrasting crustal structures (*cf.* Figs 5c and 10c). The apparent crustal thickening beneath the northern edge of the SITF results from the lack of ray coverage and is coupled, in this model, with a higher velocity modelling artefact being introduced beneath the ridge-transform intersection (∼100 km along-profile distance in Figs 10b,c). Checkerboard testing (Fig. 11) shows that features 5-km wide × 2-km deep in size are as well resolved along the entire profile as for the *P-wave inversion model*, but are better resolved beneath the SITF in the *seeded inversion model*.

On this basis, the *density model*, which has constraint from the seismic inversion results, is considered a more likely representation of true entire crustal structure along Profile P01S. Consequently, this model was, in turn, converted into a node-specified model with distinct layer boundaries imposed (Fig. 12a). This model (henceforth the *forward gravity model*) was forward point-to-point ray traced (Fig. 12b) following the same process as adopted for the *P-wave inversion model* (Fig. 9) without adjusting any layer velocity or interface to appraise the fit. The *forward gravity model* has a significantly improved fit. The largest misfits occur for OBSs 115 and 121 only, which are located on relative flat seabed immediately to the north and south of the SITF wider bathymetric depression. The fit for OBS 001 is greatly improved (*cf.* Figs 9e and 12e), with the calculated traveltimes now arriving ∼50–200 ms early (set in the context of the 75 ms pick error) depending on offset, suggesting again that the gravity-derived crustal structure of the SITF is more likely.

All possible PmP ray paths through the model were also traced and their arrival times compared with the sparsely observed arrivals. Examples are shown in Fig. 12 for OBSs 113 (sited on 0-Myr-old oceanic crust ∼25 km to the north of the SITF), 125 (sited on the continental slope) and 001 (sited at the ridge-transform intersection). This modelling goes someway to explaining why PmP arrivals, if there is a sharp interface at the base of crust, are not observed at OBSs sited on oceanic crust, as this modelling predicts that they would arrive either coincident with the water waves or very shortly after the first arriving crustal phases and, thus, be obscured by their wave trains.

8 MODEL SIMILARITY AND UNIQUENESS

The *P-wave inversion, density* and *forward models* are generally consistent within their associated uncertainties, except for the deeper crustal and uppermost mantle structure beneath the continental slope and beneath the SITF where ray coverage is limited. As such, these models should be considered together, each informing different aspects of either velocity–depth structure or interface depth and characteristics. Together, though, they provide a unique view of the subsurface geological structure along a transect along the Mid-Cayman Spreading Centre, its intersection with the Swan Islands transform fault zone and across the Honduran continental margin. The features of these models will now be discussed in the context of oceanic crustal accretionary processes, the characteristics of ridge-transform intersections, and the evolution of transform continental margins. For this purpose, we assume that the 7.5 km s^{-1} velocity contour acts as a proxy for the base of crust along the

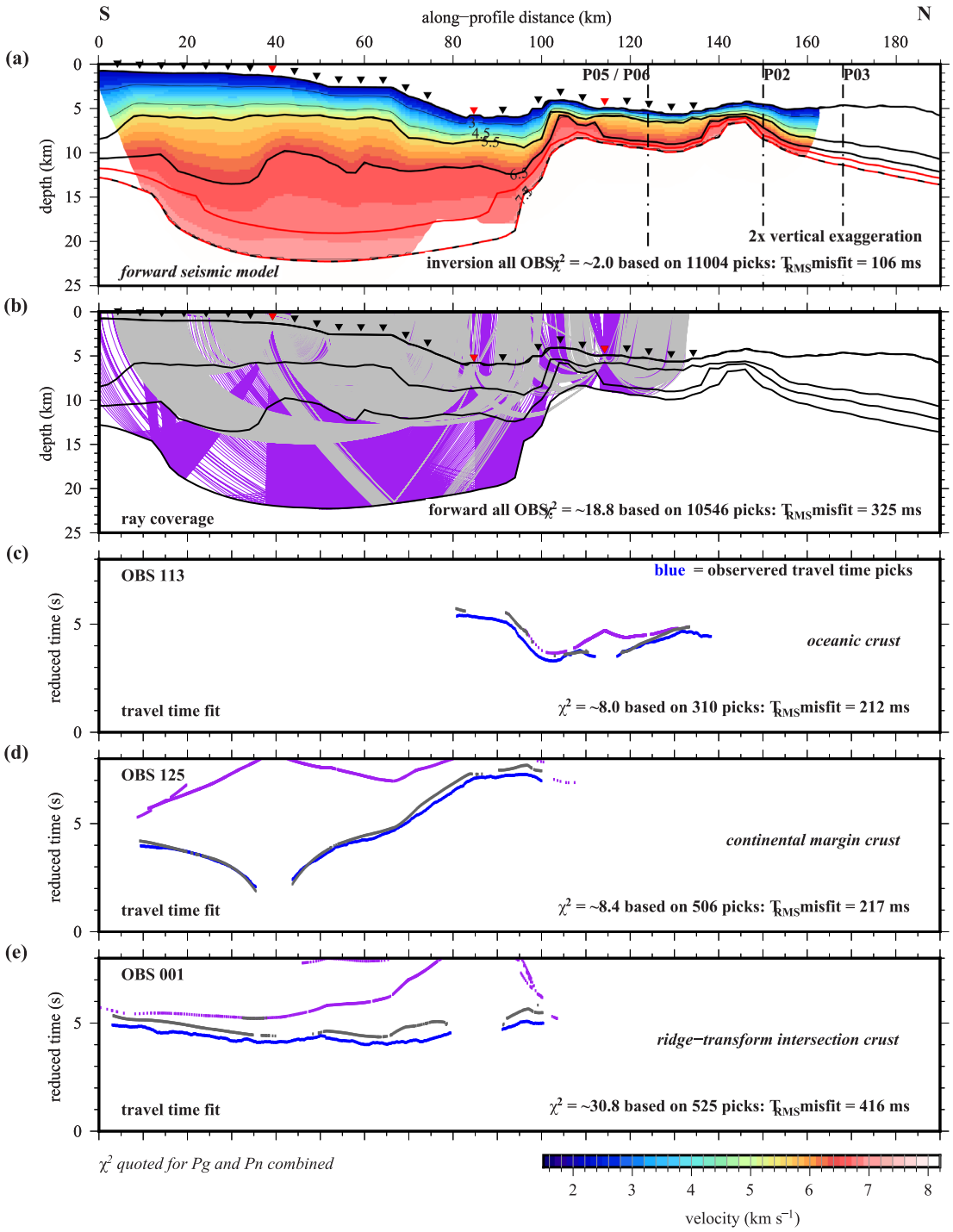

Figure 9. Forward ray tracing to constrain the Moho and SITF. (a) *Forward seismic model* derived from the *P-wave inversion model* and using the 5.5 km s^{-1} contour to mark the boundary between the upper and lower crust. *P-wave inversion model'* 7.0 and 7.5 km s^{-1} contours are shown for reference as solid and dashed red lines respectively. OBS locations are shown (black inverted triangles), with OBSs 001, 113 and 124 highlighted in red. *CAYSEIS* Profiles P05/P06, P02 and P03 (left to right) are marked by the dot-dashed lines. (b) Ray diagram for OBSs 001, 113 and 125, showing traveltimes point-to-point traced as both Pg and Pn phases (grey ray paths), and a predictive trace of where PmP arrivals (purple ray paths) should be observed. See text for discussion. (c–e) Time-distance graphs for OBSs 113 (oceanic crust), 125 (continental crust) and 001 (ridge-transform intersection crust) showing the ray traced arrivals (Pg and Pn—grey; PmP—purple) compared with observed arrivals (blue) with dot size set to pick error. The predicted PmP arrivals are shown on the corresponding data sections in Fig. 3. χ^2 fit, the root-mean-square misfit (T_{RMS}) and the number of traveltime picks are labelled for each stage.

entire profile. We also base crustal type identifications on a series of velocity–depth profiles taken at 5 km intervals through both forward and inverse *P*-wave models (Figs 13a–e), and by comparing them to standard compilations [e.g. fracture zones—Minshull *et al.* (1991): oceanic crust–White (1979, 1984), as summarized in White *et al.* (1992) and Grevemeyer *et al.* (2018b); continental crust—as summarized in Peirce *et al.* (1996) and Greenroyd *et al.* (2007, 2008)].

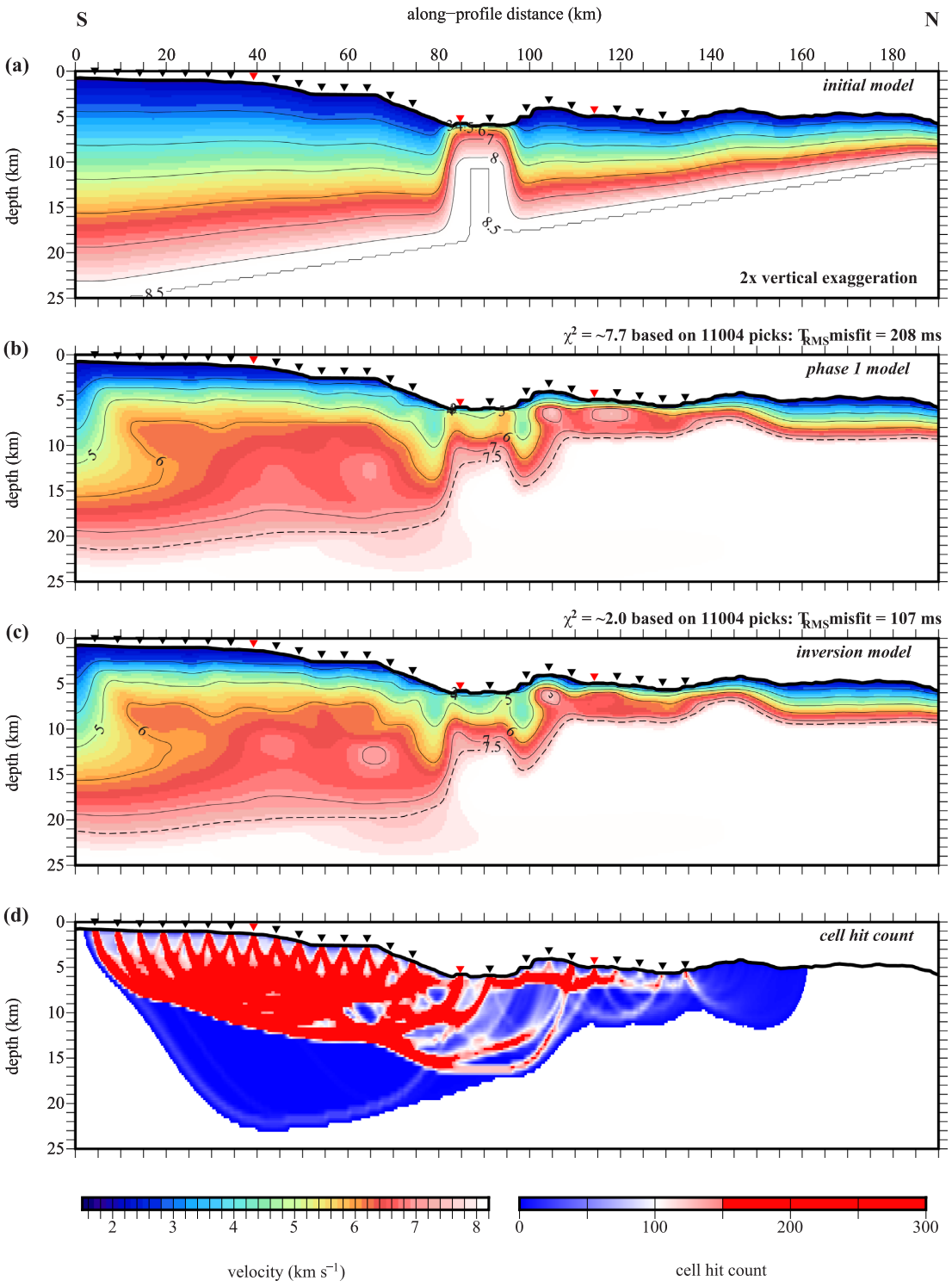

Figure 10. Inversion modelling of SITF crustal structure using a seeded initial model based on the *density model*. (a) *P-wave initial model*. (b) *Phase 1 interim model*. (c) Best-fitting *seeded inversion model*. Approach and inversion parameters were kept as summarized in Table 1. χ^2 fit, the root-mean-square misfit (T_{RMS}) and the number of traveltime picks are labelled for each stage. Velocity contours are plotted at 1.0 km s^{-1} intervals, together with the 7.5 km s^{-1} contour used as a proxy for base of crust. (d) Cell hit count indicatively showing ray coverage used as the mask in Fig. 11. In all parts, OBS locations are marked by inverted black triangles, with OBSs 001, 113 and 125 highlighted in red.

8.1. *P-wave* inversion model

The *P-wave inversion model* (Fig. 14a) has a generally smooth velocity pattern that largely mirrors the seabed topographic highs and lows. Based on velocity–depth profiles the model can be divided into three primary domains: (i) continental crust to the south of the SITF (<40 km along-profile distance—Figs 13a and b); (ii) thinned continental slope crust and SITF (>40 km to ~100 km—Fig. 13b) and (iii) oceanic crust to

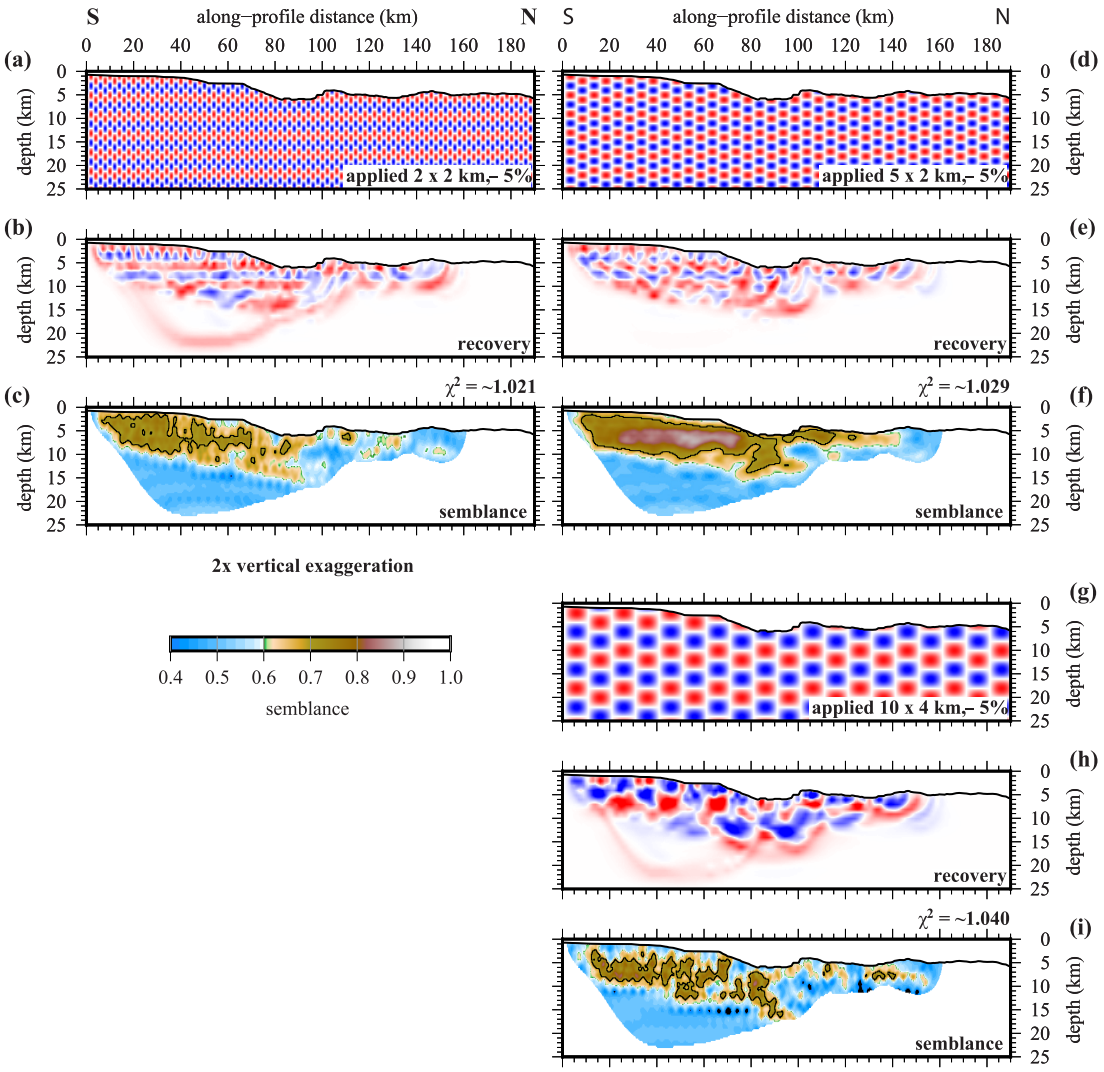

Figure 11. Checkerboard resolution testing of the *seeded inversion model*. (a) Checkerboard applied to the *seeded inversion model* with a 2 × 2 km pattern size and 5 per cent velocity anomaly. (b) Recovered checkerboard. (c) Semblance masked by ray coverage. A semblance of 0.7 is used as the good resolution threshold. χ^2 fit is annotated. A good resolution is achieved for the top ~5–7 km of the continental crust. (d–f) Checkerboard testing with a 5 × 2 km and 5 per cent velocity anomaly checkerboard. A good resolution is achieved to ~10 km depth in the continental crust and a better resolution is achieved beneath the SITF, and to ~3–5 km beneath the MCSC. (g–i) Checkerboard testing with a 10 × 4 km and 5 per cent velocity anomaly checkerboard.

the north (>100 km—Figs 13c–e). The oceanic domain can further be subdivided based on apparent crustal thickness variation and velocity within the upper crust: (a) ridge tip/inside corner (~100–110 km—Fig. 13c); (b) magma rich (~110–125 km—Fig. 13d) and (c) magma poor (~>125 km—Fig. 13e).

To the south of the SITF the continental crust appears to be ~22-km thick until, at an along-profile distance of ~40 km, it starts to thin coincident with the transition from shelf to slope at the seabed (Fig. 7a). A velocity of 2.5 km s^{-1} at the seabed suggests sediment cover in this section of the model, with the transition between upper and lower crust marked by the 6.0 km s^{-1} velocity contour. The upper crustal velocity–depth structure is consistent, to a depth of 6–7 km subseabed, and implies that the variation in crustal thickness is due to thinning of the lower crust. Due to the lack of ray coverage at the most southerly end of the model, gravity modelling better constrains the crustal thickness at ~25 km.

Oceanic-type crust at the ridge-transform intersection (Fig. 13c) appears to be thinner (~3 km) than beneath the SITF (~5 km—Fig. 13b), and the MCSC adjacent to the north (~3–4 km—Fig. 13d), and equivalent to that beneath the mid-segment (~3 km—Fig. 13e). Velocity–depth profiles for the SITF (Fig. 13b) show it to be characteristically oceanic, based on the 0–7 Ma crustal envelope of White *et al.* (1992).

Moving northwards, the thickest oceanic crust (~4 km) between ~110 and ~125 km along-profile distance (Figs 14a & 13d) also has a higher velocity at shallower depths and slower velocity at deeper depths than observed elsewhere along the oceanic part of the profile. The additional crust appears to be related to a thicker lower crust and suggests that the crust formed under more magma rich conditions. Further north, the velocity–depth structure is quite variable laterally for the remaining ~40 km along-profile (Fig. 13e), with an average crustal thickness of ~3 km and structural variation mirroring the seabed topography. In general, at the seafloor the velocity varies between 2.7 and 4.0 km s^{-1}, with the upper-to-lower crust transition characterized by the 5.5 km s^{-1} contour marking a change in vertical velocity gradient. The lower oceanic crust, on average, has velocities higher than 6.0 km s^{-1}.

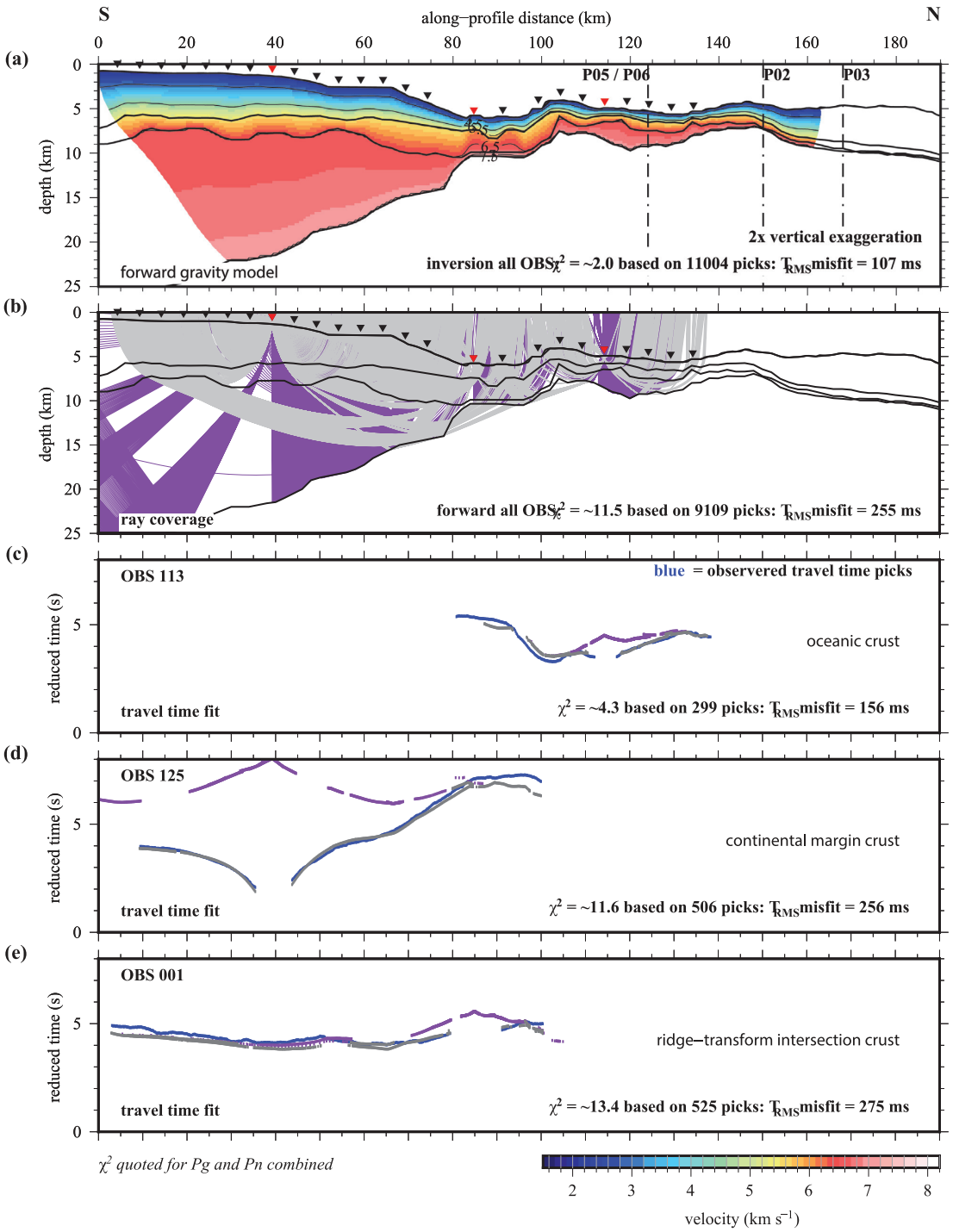

Figure 12. Forward ray tracing to constrain the Moho and SITF. (a) *Forward model* derived from the *seeded inversion model* and using the 5.5 km s^{-1} contour to mark the boundary between the upper and lower crust and the 7.5 km s^{-1} contour as a proxy for the base of crust. OBS locations are shown (black inverted triangles), with OBSs 001, 113 and 124 highlighted in red. *CAYSEIS* Profiles P05/P06, P02 and P03 (left to right) are marked by the dotted–dashed lines. (b) Ray diagram for OBSs 001, 113 and 125, showing traveltimes point-to-point traced as both Pg and Pn phases (grey ray paths), and a predictive trace of where PmP arrivals (purple ray paths) should be observed. See text for discussion. (c–e) Time–distance graphs for OBSs 113 (oceanic crust), 125 (continental crust) and 001 (ridge-transform intersection crust) showing the ray traced arrivals (Pg and Pn—grey; PmP—purple) compared with observed arrivals (blue) with dot size set to pick error. χ^2 fit, the root-mean-square misfit (T_{RMS}) and the number of traveltime picks are labelled for each stage. Note the better fit achieved when compared to that for the *P-wave inversion model* shown in Fig. 9.

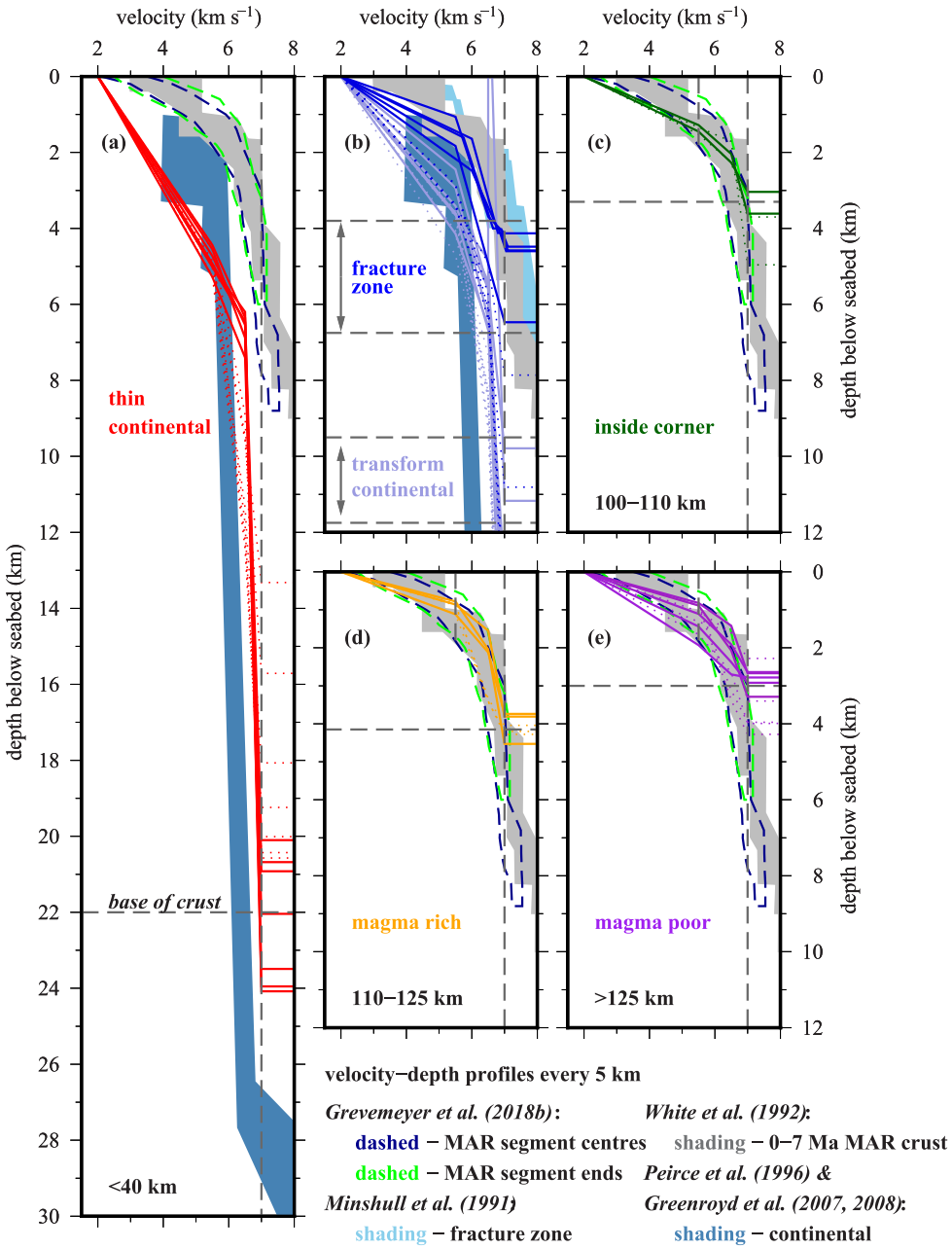

Figure 13. *P-wave forward* (solid lines) and *inversion* (dotted lines) *model* velocity–depth profiles. 1-D profiles, extracted at 5 km intervals, are colour-coded by setting along-profile: (a) continental crust; (b) transform continental and fracture zone crust; (c) ridge-transform intersection; (d) magma rich and (e) magma poor oceanic crustal formation. Average crustal thicknesses are marked (horizontal grey dashed lines). Profiles are compared to the Atlantic crustal velocity–depth envelopes of White *et al.* (1992) (grey shaded) and Grevemeyer *et al.* (2018b) (blue dashed = MAR segment centre crust; green dashed = MAR segment end crust), continental crustal (blue shaded) compilations of Peirce *et al.* (1996) and Greenroyd *et al.* (2007, 2008), and the fracture zone compilation (light blue shaded) of Minshull *et al.* (1991).

8.2 Density model

The *density model* (Fig. 8b) shows a contrast in structure between the continental and oceanic regions as would be expected and, on the whole, a higher density throughout the crust than predicted from inversion modelling. Similar to the *P-wave inversion model*, the gravity modelling suggests that the section of the MCSC surveyed divides along-axis into two main structural styles. The rift tip/segment end and the mid-segment zones are underlain by a thinner crust with a thicker, lower-density upper crustal section, while the zone in between has not only a thicker crust, but also a higher density crust, with a much thinner upper crustal section. Grevemeyer et al.'s (2018a) modelling of Profiles P05 and P06, which extrapolate across-axis through this zone, suggests that this section of the MCSC is currently in a magma dominated phase of accretion, and is consistent with the modelling along-axis presented here.

To the south of the SITF the *density model* suggests that the margin formed by an effectively constant period of extension, thinning the crust from ~25-km thick to ~10-km thick over a distance of

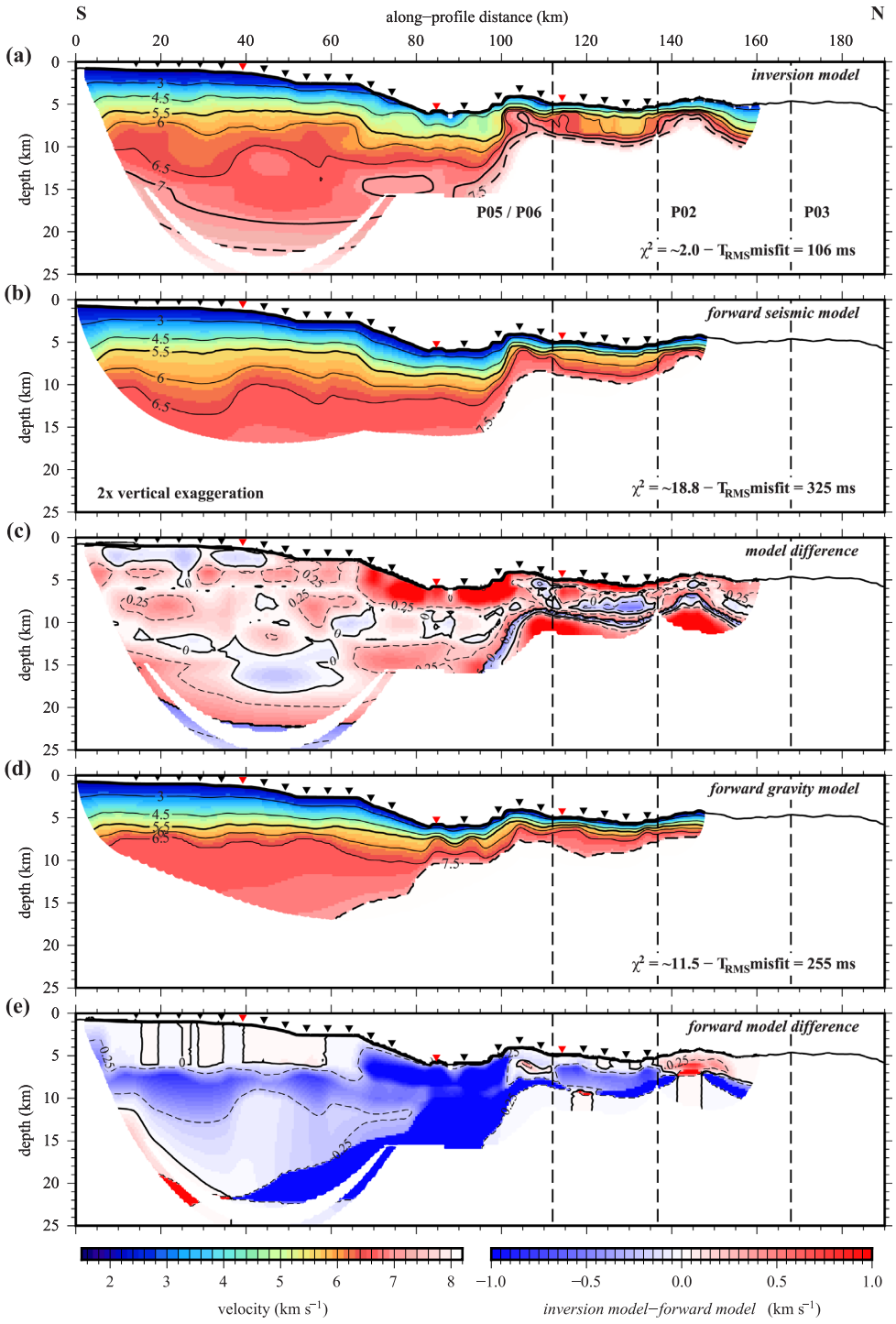

Figure 14. Comparison between *P*-wave velocity–depth models resulting from inversion and forward approaches to modelling. (a) *P-wave inversion model*. (b) *Forward seismic model*. (c) Calculated velocity difference between the two models, contoured at 0.25 km s^{-1} intervals. (d) *Forward gravity model*. (e) Calculated velocity difference between the *forward seismic model* and the *forward gravity model*, contoured at 0.25 km s^{-1} intervals. See text for discussion. The 5.5 km s^{-1} velocity contour marks the transition from upper-to-lower crust and the 7.5 km s^{-1} contour (dashed) denotes the Moho. OBS locations are shown (black inverted triangles), with OBSs 001, 113 and 125 highlighted in red. *CAYSEIS* Profiles P05/P06, P02 and P03 (left to right) are marked by the dashed lines. χ^2 fit and root-mean-square misfit (T_{RMS}) are labelled.

~65 km. This thinning is largely accommodated within the lower crust where, in turn, the density increases as the crust thins. A matching lateral relative increase in density within the mantle is also modelled, which continues northwards along the entire P01 profile. This is required to model the longer-wavelength component of the FAA.

The most prominent feature of the *density model* lies beneath the SITF where a region of much higher density is required to

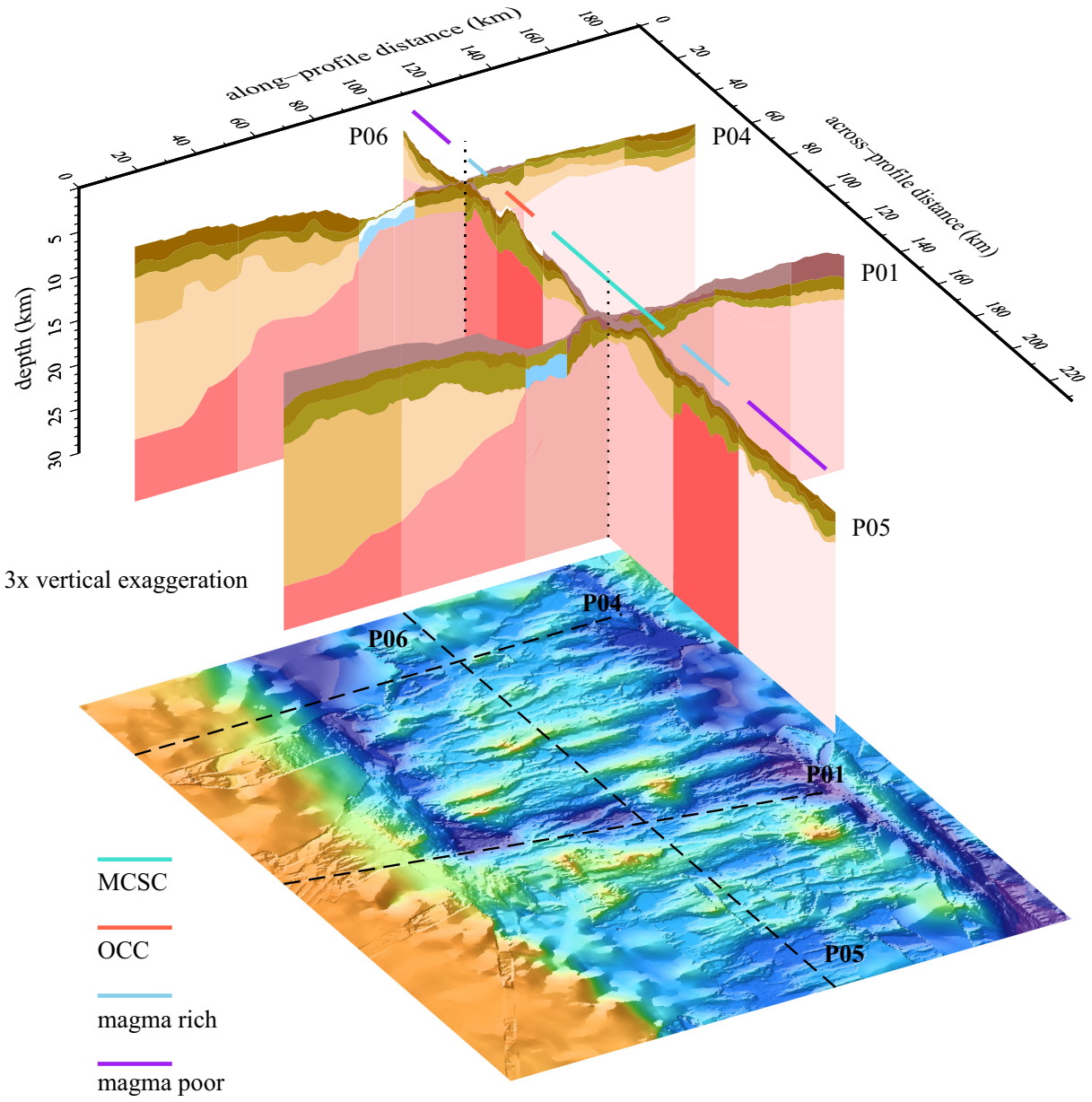

Figure 15. Fence diagram of gravity models for *CAYSEIS* Profiles P01, P04 and P05/P06 showing the correspondence at intersection/extrapolation points, the crustal structure of the SITF, and the along-SITF variation in adjacent continental margin structure that suggests a change in evolution from transtensional to more strike-slip tectonism at ∼10 Ma. The temporal variation in crustal formation, from magma rich to magma poor, is shown by the blue and purple bars respectively, and the location of the MCSC and a relic OCC off-axis by the turquoise and red bars. The location of these profiles, relative to the bathymetry (below), is shown by dashed lines.

resolve the remaining misfit. This feature can be interpreted in two ways: (i) that the crust beneath the SITF is ∼2–3-km thick and underlain by an upper mantle that has been serpentinized, most likely by water influx and circulation along the faults and fractures that comprise the ridge-transform intersection zone or (ii) that the crust is ∼4–5-km thick with the lower crust comprising altered or exhumed lithologies. The density structure above and the mantle density below suggest the latter may be more likely. Either way, the zone of anomalous density is ∼15-km wide, underlying the entire width of the ridge-transform intersection zone, and not just the much narrower width of the bathymetric depression that is identified as the SITF at the seabed.

8.3. Differences between inversion and gravity models

Perhaps the best way to consider the differences between the inversion- and gravity-derived models is to consider the differences between the forward ray-trace models constructed from them. First, to test this approach a comparison is made between the *P-wave inversion* (Fig. 14a) and *forward seismic* (Fig. 14b) *models* by calculating the velocity difference between them throughout the model space (Fig. 14c). This shows that the conversion process has resulted in a forward model that only has velocities generally <0.25 km s^{-1} higher (within the modelling error) than its inversion equivalent, suggesting that the approach is valid. The primary difference observed, where the velocity difference exceeds 0.25 km s^{-1}, lies at

the SITF, but, even then, is largely constrained to the upper 2–3 km below seabed. The primary negative-positive bands result from how the layer boundaries in the *forward seismic model* were imposed using smoothed velocity contours. The *forward gravity model* (Fig. 14d) was constructed using its constituent polygon perimeters, and conversion of its densities to velocities using the standard relationships outlined in Section 6.2. This model was then subtracted from the *forward seismic model* to create the difference between the forward models shown in Fig. 14(e). As might be expected, what this shows is that the *forward gravity model* is consistent (<0.25 km s^{-1} difference) with the *forward seismic model* in the upper crust beneath the continental shelf, and in the upper crust along the entire MCSC surveyed. The primary differences, where the *forward gravity model* results in velocities >0.5 km s^{-1} higher, clearly correlate with maximum depth limits of areas of highest ray coverage (*cf*. Figs 14e and 5d), except in the vicinity of the steepest parts of the continental slope and the breadth of the SITF. Here the velocity difference is $\sim$1.0 km s^{-1} with, perhaps its most interesting characteristic being a steep vertical transition implied at the ridge-transform intersection, and higher velocity within the entire crust and uppermost mantle beneath the SITF.

9 DISCUSSION

9.1. Oceanic crustal accretion at the Mid-Cayman Spreading Centre

The modelling of all *CAYSEIS* profiles conducted to date (Harding *et al.* 2017; Van Avendonk *et al.* 2017; Grevemeyer *et al.* 2018a; Peirce *et al.* 2019b) concludes that oceanic crustal formation at the MCSC is dependent on temporal fluctuations in magma supply, where magma rich accretion swaps to magma poor spreading over a time frame of several million years, and where magma may arrive in pulses to specific locations along the spreading axis, rather than consistently along the entire segment length (Harding *et al.* 2017). For example, Harding *et al.* (2017) propose that, 2 Ma, a pulse of magmatism initiated the axial flank Von Damm hydrothermal vent field near the summit of the Mt Dent oceanic core complex. Furthermore, Van Avendonk *et al.* (2017) conclude that axial magmatism has been episodic for the last 20 Myr, and that the northern section of the MCSC axial valley can be divided into multiple magmatic-tectonic segments. Based on bathymetry analysis, Haughton *et al.* (2019) hypothesize that magma intrusions have propagated southward along the northern section of the MCSC to the Mt Dent OCC where they crosscut its detachment, and possibly deactivate slip along it. Consequently, the Mt Dent OCC may lie at the boundary between adjacent currently magmatic segments of the MCSC.

Grevemeyer *et al.* (2018a) show that seafloor spreading at the MCSC switches between 2-Myr-long periods of magma rich and magma poor oceanic crustal formation, during which serpentinized mantle is also exhumed. However, even though the eastern and western flanks share similar features, the durations of periods of magma rich versus magma poor spreading are distinctly different, suggesting that not only is accretion episodic, but also that it is asymmetric. Our observations suggest that magmatic accretion may not only be episodic in the across-axis direction (Grevemeyer *et al.* 2018a), but is also similarly focused, or episodic, in the along-axis direction, with the ridge currently magmatically accreting as far south as the ridge-transform intersection, where the transition from one to the other in crustal structure terms, is both laterally and vertically rapid. Such a focused magma delivery along-axis, where the junctions between magma rich segments host OCCs, is consistent with the dredging of both ultramafic and mafic gabbroic rocks (Hayman *et al.* 2011), and implies that regions of tectonic and magmatically formed crust may be interdispersed.

Consistent with previous studies conducted at the ultraslow MCSC (e.g. Ewing *et al.* 1960; White *et al.* 2001; ten Brink *et al.* 2002; Harding *et al.* 2017; Van Avendonk *et al.* 2017; Grevemeyer *et al.* 2018a; Peirce *et al.* 2019b), our results show a generally thin oceanic crust ($\sim$3–4-km thick) along the southern section of the ridge axis, suggesting that it is forming currently under less magmatic conditions than the northern section (Fig. 7c). The apparent absence of PmP arrivals observed amongst multiple *CAYSEIS* profiles also suggests that the crust-mantle boundary is a transition zone, both on- and off-axis, which could result from alteration of the lower crust/upper mantle by fluid flow along faults and fractures (Peirce *et al.* 2019b).

Based on our modelling, the transition between spreading ridge and transform fault zone appears to be abrupt, with no evidence of magma leakage as Grevemeyer *et al.* (2021) propose. However, the profile crossed the active transform domain in the vicinity of the ridge-transform intersection, and not where the impact of a second phase of magmatism would be most prominent (Grevemeyer *et al.* 2021). Consequently, the ridge-transform zone is characterized with a more normal upper oceanic crustal structure. Modelling also suggests that the crust here is thin and has predominantly upper oceanic crustal density and velocity characteristics, and that either the lower crust is below seismic resolution in thickness at this depth and is underlain by a serpentinized upper mantle, or that the lower crust has been tectonically sheared, fractured and hydrated.

9.2 Swan Islands transform ocean–continental margin

The combined seismic and gravity modelling shows that the crust beneath the Swan Islands (Honduran) margin is continental in lithology and relatively thin at $\sim$20–25-km-thick below the shelf, thinning beneath the $\sim$60-km-wide slope region to $\sim$14-km thick and then more rapidly over $\sim$5-km to $\sim$10-km thick at the southern edge of the SITF. This represents thinning of more than 50 per cent over a distance of $\sim$65 km. Neither of the seismic or gravity models suggests multistage rifting/extension during margin evolution, unlike that observed to the west along Profile P04 (Peirce *et al.* 2019b).

However, several studies conducted at margins in stage 3 (passive stage) of their evolution suggest that continental crustal thinning can be quite variable between transform margins, where gravity and wide-angle seismic models suggest that the crust can thin significantly over a distance of less than 10–40 km. For example, the Barents Sea-Svalbard (Feleide *et al.* 1991), Ghana (Edwards *et al.* 1997), Grand Banks (Keen *et al.* 1990), North Atlantic (Fox & Gallo 1986) and Exmouth Plateau (Lorenzo *et al.* 1991) margins exhibit continental crustal thinning over zones of 10–20-, 15- and 40-km wide, respectively. Unlike the Ghana ocean–continent boundary (Edwards *et al.* 1997) there is no evidence of a region of high density (3100 kg m^{-3}), high velocity (5.8–7.3 km s^{-1}) or high magnetization (1.10–1.25 A m^{-1}) beneath the Swan Islands margin, suggesting that any tectonically facilitated alteration of the crust and/or upper mantle material is constrained within the SITF alone. Here, our models suggest that the SITF, at least beneath profile P01S, is a narrower zone of deformation and alteration than observed beneath Profile P04 located 10 Ma off-axis. We explain the high-density anomaly beneath the SITF to result from water ingress into the lower crust and uppermost mantle through the fracture system.

9.3 Margin perspective

A 3-D perspective on Swan Islands margin and MCSC crustal structure is provided by the fence diagram of Profiles P01, P04, P05 and P06 shown in Fig. 15. The along-axis variability in magma rich and magma poor spreading conditions is particularly evident, as is the temporal variation across axis. What is perhaps more striking is that the sections of the ridge axis that have a richer supply of magma and those with a poorer, appear to persist over geological time, since even though the MCSC 10 Myr ago was less magmatic overall than the present day, even then the pattern of along axis variation is consistent with that observed currently, which is also mirrored in the crustal thickness. This observation suggests the segmentation is driven predominantly by perturbations in magma production and delivery from the deeper mantle.

The fence diagram also shows the contrasting margin evolution styles between the present day and at 10 Ma. When considered in the context of the seabed bathymetry, Profile P04 is located where the SITF transitions from being wide and deep to being a shallower and much narrower feature at the seabed, with this contrasting structure extending to depth throughout the crust. The transtensional extension proposed by Peirce *et al.* (2019b) to explain the step-like thinning of the crust also results in the greater width of the SITF along the older parts of margin, and implies a change in plate motion occurred around ∼10 Ma. Now, the Swan Islands margin appears to actively evolving in a purely strike-slip fashion.

10 CONCLUSIONS

Velocity–depth and density–depth models for the Swan Island transform margin have been presented for an ∼165-km-long transect that also traverses the present-day Mid-Cayman Spreading Centre and the ridge-transform intersection. These models are consistent and robustly tested and we summarize their interpretation as follows:

(1) The oceanic crust accreted at the ultraslow MCSC is ∼3–4-km-thick and most likely is forming during a period of predominantly magma rich spreading at the southern end of the segment, with a variation in magma supply evident along-axis.

(2) The location of OCCs appears to define the boundaries between more and less magmatic sections of the MCSC suggesting, in turn, focused magma delivery to the ridge axis, that also waxes and wanes over time.

(3) Magma supply within a magma rich section appears consistent along its length such that the crustal thickness at the southern ridge tip is equivalent to that at the centre of the segment section to its north.

(4) There is no evidence for magma leakage from the spreading ridge into the transform zone.

(5) The SITF is an ∼15-km-wide zone, bound to the south by a sharp transition between oceanic- and continental crusts and to the north by an abrupt change in crustal thickness to that observed beneath the MCSC.

(6) Beneath the SITF lies a region of higher density which most likely represents a broad zone of alteration caused by influx of water.

(7) The continental crust beneath the Honduran margin is thin at 25 km, and thins consistently by a further ∼15 km over a distance of ∼65 km towards the SITF.

(8) The Swan Island stage 2 (drifting) transform continental margin is characterized by a ∼15-km-wide predominantly strike-slip system, that appears to have had a transtensional component more than 10 Myr ago.

ACKNOWLEDGMENTS

We thank the officers, engineers and crew of the F/S Meteor for their support during the M115 *CAYSEIS* cruise. Funding for this project was provided by the UK's Natural Environment Research Council (NERC) under grant NE/K011162/1 to Durham University, the US National Science Foundation (NSF) under grant OCE-1356895 to the University of Texas Austin (UTIG), and to GEOMAR by the German Research Foundation (DFG). The wide-angle seismic data were recorded with instruments provided by UTIG and GEOMAR, as well as NERC's Ocean-Bottom Instrumentation Facility (Minshull *et al.* 2005). We thank their technical teams for their professional support. The ship-based gravimeter was provided by the NERC's National Marine Equipment Facility, together with its installation technical support. All figures were prepared using the Generic Mapping Tools (GMT) package (Wessel & Smith 1998). The manuscript of this paper is deposited in Durham University's open access publication repository, Durham Research Online (DRO—dro.dur.ac.uk). We thank our two reviewers, Milena Marjanović and Michele Paulatto, for their entirely positive views on our manuscript and the quality of the research presented.

DATA AVAILABILITY

The seismic data used in this study are available at the Academic Seismic Portal at UTIG (www-udc.ig.utexas.edu/sdc), the World Data Center PANGAEA (www.pangaea.de), and the British Oceanographic Data Centre (www.bodc.ac.uk).

REFERENCES

Basile, C., Mascle, J., Benkhelil, J. & Bouillin, J.-P., 1998. Geodynamic evolution of the Cote d'Ivoire-Ghana transform margin: an overview of Leg 159 results, in *Proceedings of the Ocean Drilling Program, Scientific Results,* Vol. **159,** pp. 101–110, eds Mascle, J., Lohmann, G.P. & Moullade, M., Ocean Drilling Program.

Blarez, E. & Mascle, J., 1988. Shallow structure and evolution of the Ivory Coast and Ghana transform margin, *Mar. Petr. Geol.,* **5,** 54–64.

Carlson, R.L. & Miller, D.J., 2003. Mantle wedge water contents estimated from seismic velocities in partially serpentinized periodotites, *Geophys. Res. Letts.,* **30**(5), doi:10.1029/2002GL016600.

Carlson, R.L. & Raskin, G.S., 1984. Density of the ocean crust, *Nature,* **311,** 555–558.

Christeson, G.L., Gulick, S.P., Van Avendonk, H.J., Worthington, L.L., Reece, R.S. & Pavlis, T.L., 2010. The Yakutat terrane: dramatic change in crustal thickness across the Transition fault, Alaska, *Geology,* **38**(10), 895–898.

Christensen, N.I. & Mooney, W.D., 1995. Seismic velocity structure and composition of the continental crust: a global view, *J. geophys. Res.,* **100**(B6), 9761–9788.

Connelly, D.P., Copley, J.T., Murton, B.J., Stansfield, K., Tyler, P.A., German, C.R., Van Dover, C.L., Amon, D., Furlong, M., Grindlay, N. & Hayman, N., 2012. Hydrothermal vent fields and chemosynthetic biota on the world's deepest seafloor spreading centre, *Nat. Commun.,* **3,** 620.

Dalziel, I.W.D. & Dewey, J.F., 2019. The classic Wilson cycle revisited, in *Fifty Years of the Wilson Cycle Concept in Plate Tectonics,* Vol. **470,** pp. 19–38, eds Wilson, R.W., Houseman, G.A., McCaffrey, K.J.W., Doré, A. G. & Buiter, S. J. H., Geol. Soc. Spec. Pub.

DeMets, C., Mattioli, G., Jansma, P., Rogers, R., Tenorio, C. & Turner, H.L, 2007. Present motion and deformation of the Caribbean plate: constraints from new GPS geodetic measurements from Honduras and Nicaragua, *Geol. Soc. Am. Spec. Pub.,* **428,** 21–36.

Detrick, R.S., White, R.S. & Purdy, G.M, 1993. Crustal structure of North Atlantic fracture zones, *Rev. Geophys.,* **31,** 439–458.

Dick, J.J.B., Lin, J. & Schouten, H., 2003. An ultraslow-spreading class of ocean ridge, *Nature,* **426,** 405–411.

Edwards, R.A., Whitmarsh, R.B. & Scrutton, R.A, 1997. The crustal structure across the transform continental margin off Ghana, eastern equatorial Atlantic, *J. geophys. Res.,* **102**(Bl), 747–772.

Escartin, J., Hirth, G. & Evans, B., 1997. Nondilatant brittle deformation of serpentinites: implications for Mohr-Coulomb theory and the strength of faults, *J. geophys. Res.,* **102,** 2897–2913.

Ewing, J., Antoine, J. & Ewing, M., 1960. Geophysical measurements in the western Caribbean Sea and in the Gulf of Mexico, *J. geophys. Res.,* **65,** doi:10.1029/JZ065i012p04087.

Feleide, J.I., Gudlaugsson, S.T., Eldholm, O., Myhre, A.M. & Jackson, H.R., 1991. Deep seismic transects across the sheared western Barents Sea-Svalbard continental margin, *Tectonophysics,* **189,** 73–89.

Fox, P.J. & Gallo, D.G., 1986. The geology of North Atlantic transform plate boundaries and their aseismic extensions, in *DNAG The Geology of North America: The western North Atlantic Region,* Vol. **M,** pp. 157–172, eds Vogt, P.R. & Tucholke, B.E., Geological Society of America.

Francheteau, J. & Le Pichon, X., 1972. Marginal fracture zones as structural framework of continental margins in South Atlantic Ocean, *AAPG Bull.,* **56,** 991–1007.

Gadd, S.A. & Scrutton, R.A., 1997. An integrated thermomechanical model for transform continental margin evolution, *Geo. Mar. Letts.,* **17,** 21–30.

Greenroyd, C.J., Peirce, C., Rodger, M., Watts, A.B. & Hobbs, R.W., 2007. Crustal structure of the French Guiana margin, West Equatorial Atlantic, *Geophys. J. Int.,* **169,** 964–987.

Greenroyd, C.J., Peirce, C., Rodger, M., Watts, A.B. & Hobbs, R.W., 2008. Demerara Plateau – the structure and evolution of a transform passive margin, *Geophys. J. Int.,* **172,** 549–564.

Grevemeyer, I., Dannowski, A., Hayman, N.W., Peirce, C. & Van Avendonk, H., 2016. *CAYSEIS* – magma-starved oceanic crustal accretion and transform margin formation in the Cayman Trough revealed by seismic and seismological data, FS Meteor M115 cruise report (unpublished), pp. 92.

Grevemeyer, I., Hayman, N.W., Peirce, C., Schwardt, M., Van Avendonk, H., Dannowski, A. & Papenberg, C., 2018a. Episodic magmatism and serpentinized mantle exhumation at an ultraslow spreading centre, *Nat. Geosci.,* **11,** 444–448.

Grevemeyer, I., Ranero, C.R. & Ivandic, M., 2018b. Structure of oceanic crust and serpentinization at subduction zones, *Geosphere,* **14**(2), 395–418.

Grevemeyer, I., Hayman, N.W., Lange, D., Peirce, C., Papenberg, C., Van Avendonk, H.J.A., Schmid, F., Gómez de la Peña, L. & Dannowski, A., 2019. Constraining the maximum depth of brittle deformation at slow- and ultraslow-spreading ridges using microseismicity, *Geology,* **47,** 1069–1073.

Grevemeyer, I., Rüpke, L.H., Morgan, J.P., Iyer, K. & Devey, C.W., 2021. Extensional tectonics and two-stage crustal accretion at oceanic transform faults, *Nature,* **591,** 402–407.

Harding, J.L., Van Arendonk, H.J.A., Hayman, N.W., Grevemeyer, I. & Peirce, C., 2017. Magmatic-tectonic conditions for hydrothermal venting on an ultraslow-spread oceanic core complex, *Geology,* **45,** 839–842.

Haughton, G., Hayman, N.W., Searle, R.C., Le Bas, T. & Murton, B.J., 2019. Volcanic-tectonic structure of the tent oceanic core complex in the ultraslow Mid-Cayman Spreading Center determined from detailed seafloor investigation, *Geochem. Geophys. Geosyst.,* **20,** 1298–1318.

Hayman, N.W., Grindlay, N.R., Perfit, M.R. & Mann, P., 2011. Oceanic core complex development at the ultraslow spreading Mid-Cayman Spreading Centre, *Geochem. Geophys. Geosyst.,* **12**(3), doi: 10.1029/2010GC003240.

Holcombe, T.L. & Sharman, G.F., 1973. Post-Miocene Cayman Trough evolution: a speculative model, *Geology,* **11,** 714–717.

Keen, C.E., Kay, W.A. & Roest, W.R., 1990. Crustal anatomy of a transform continental margin, *Tectonophysics,* **173,** 527–544.

Kuna, V.M., Nábělek, J.L. & Braunmiller, J., 2019. Mode of slip and crust–mantle interaction at oceanic transform faults, *Nat. Geosci.,* **12,** 138–142.

Lavier, L.L. & Manatschal, G., 2006. A mechanism to thin the continental lithosphere at magma-poor margins, *Nature,* **440**(7082), 324–328.

Leroy, S., Mauffret, A., Patriat, P. & Mercier de Lepinay, B., 2000. An alternative interpretation of the Cayman Trough evolution from a re-identification of magnetic anomalies, *Geophys. J. Int.,* **141,** 539–557.

Lorenzo, J.M. & Vera, E.E., 1992. Thermal uplift and erosion across the continent-ocean transform boundary of the Southern Exmouth Plateau, *Earth planet. Sci. Lett.,* **108,** 79–82.

Lorenzo, J.M., Mutter, J.C., Larson, R.L.and &the Northwest Australia Study Group, 1991. Development of the continent-ocean transform boundary of the southern Exmouth Plateau, *Geology,* **19,** 843–846.

Ludwig, J.W., Nafe, J.E. & Drake, C.L., 1970, Seismic refraction, in *The Sea,* pp. 53–84, ed. Maxwell, A.E., Wiley-Interscience.

Mascle, J., 1976. Atlantic-type continental margins – distinction of two basic structural types, *An. Acad. Bras. Cienc.,* **48,** 191–197.

Mascle, J. & Blarez, E., 1987. Evidence for transform margin evolution from the Ivory Coast-Ghana continental margin, *Nature,* **326,** 378–381.

Mascle, J., Lohmann, P. & Clift, P., 1997. Development of a passive transform margin: cote d'Ivoire-Ghana transform margin-ODP Leg 159 preliminary results, *Geo. Mar. Lett.,* **17**(1), 4–11.

Mercier De Lepinay, M., Loncke, L., Basile, C., Roest, W., Patriat, M., Maillard, A. & De Clarens, P., 2016. Transform continental margins – Part 2: a worldwide review, *Tectonophys*., **693,** 96–115.

Minshull, T.A., White, R.S., Mutter, J.C., Buhl, P., Detrick, R.S., Williams, C.A. & Morris, E., 1991. Crustal structure at the Blake Spur Fracture Zone from expanding spread profiles, *J. geophys. Res.,* **96**(B6), 9955–9984.

Minshull, T.A., Sinha, M.C. & Peirce, C., 2005. Multi-disciplinary, subseabed geophysical imaging: a new pool of 28 seafloor instruments in use by the United Kingdom Ocean Bottom Instrument Consortium, *Sea Technol.,* **46**(10), 27–31.

Müller, M.R., Minshull, T.A. & White, R.S., 2000. Crustal structure of the Southwest Indian Ridge at the Atlantis II fracture zone, *J. geophys. Res.,* **105**(B11), 25 809–25 828.

Müller, R.D., Sdrolias, M., Gaina, C. & Roest, W.R., 2008. Age, spreading rates, and spreading asymmetry of the world's ocean crust, *Geochem. Geophys. Geosyst.,* **9,** doi:10.1029/2007GC001743.

Olive, J.A., Behn, M.D. & Tucholke, B.E., 2010. The structure of oceanic core complexes controlled by the depth distribution of magma emplacement, *Nat. Geosci.,* **3**(7), 491.

Peirce, C., 2015. *CAYSEIS* – Crustal accretion and transform margin evolution at ultraslow spreading rates, FS Meteor M115 NERC cruise report (unpublished), pp 41.

Peirce, C., Whitmarsh, R.B., Scrutton, R.A., Pontoise, B., Sage, F. & Mascle, J., 1996. Cote d'Ivoire-Ghana margin: seismic imaging of passive rifted crust adjacent to a transform continental margin, *Geophys. J. Int.,* **125,** 781–795.

Peirce, C., Reveley, G., Robinson, A.H., Funnell, M.J., Searle, R.C., Simão, N.M., MacLeod, C.J. & Reston, T.J., 2019a. Constraints on crustal structure of adjacent OCCs and segment boundaries at 13° N on the Mid-Atlantic Ridge, *Geophys. J. Int.,* **217,** 988–1010.

Peirce, C., Robinson, A.H., Campbell, A.M., Funnell, M.J., Grevemeyer, I., Hayman, N.W., Van Avendonk, H.J.A. & Castiello, G., 2019b. Seismic investigation of an active ocean-continent transform margin: the interaction between the Swan Islands Fault Zone and the ultraslow-spreading Mid-Cayman Spreading Centre, *Geophys. J. Int.,* **219,** 159–184.

Prada, M., Sallares, V., Ranero, C. R., Vendrell, M. G., Grevemeyer, I., Zitellini, N. & de Franco, R.. 2014. Seismic structure of the Central Tyrrhenian basin: geophysical constraints on the nature of the main crustal domains, *J. geophys. Res.,* **119,** 52–70.

Rogers, R.D., Mann, P. & Emmet, P.A., 2007. Tectonic terranes of the Chortis block based on integration of regional aeromagnetic and geologic data, in *Geologic and Tectonic Development of the Caribbean Plate Boundary in Northern Central America,* Special Papers-Geological Society of America, Vol. **428,** pp. 66–88, ed. Mann, P., Geological Society of America.

Rosencrantz, E., Ross, M. & Sclater, J.G., 1988. Age and spreading history of the Cayman Trough as determined from depth, heat flow, and magnetic anomalies, *J. geophys. Res.,* **93**(B3), 2141–2157.

Sage, F., Basile, C., Mascle, J., Pontoise, B. & Whitmarsh, R.B., 2000. Crustal structure of the continent–ocean transition off the Côte d'Ivoire–Ghana transform margin: implications for thermal exchanges across the palaeotransform boundary, *Geophys. J. Int.,* **143,** 662–678.

Sanchez, J., Mann, P. & Emmet, P.A., 2016. Late Cretaceous–Cenozoic tectonic transition from collision to transtension, Honduran Borderlands and Nicaraguan Rise, NW Caribbean Plate boundary, in *Transform Margins: Development, Controls and Petroleum Systems,* Vol. **431,** pp. 273–297, eds Nemčok, M., Rybár, S., Sinha, S.T., Hermeston, S.A. & Ledvényiová, L., Geol. Soc. Lond. Spec. Pub.

Sandwell, D.T. & Smith, W.H.F., 2009. Global marine gravity from retracked Geosat and ERS-1 altimetry: ridge segmentation versus spreading rate, *J. geophys. Res.,* **114,** doi:10.1029/2008JB006008.

Searle, R.C., 2012. Multiple seafloor spreading modes in the Mid-Cayman Spreading Centre, in *AGU Fall Meeting*, Session OS13B-1733.

Talwani, M., Worzel, J.L. & Landisman, M., 1959. Rapid gravity computations for two-dimensional bodies with application to the Mendocino submarine fracture zone, *J. geophys. Res.,* **64,** 49–59.

Taylor, B., Goodliffe, A. & Martinez, F., 2009. Initiation of transform faults at rifted continental margins, *C.R. Geosci.,* **341,** 428–438.

ten Brink, U., Coleman, D. & Dillon, W.P., 2002. The nature of the crust under Cayman Trough from gravity, *Mar. Petrol. Geol.,* **19,** 971–987.

Todd, B.J., Reid, I. & Keen, C., 1988. Crustal structure across the southwest. Newfoundland transform margin, *Can. J. Earth Sci.,* **25,** 744–759.

Tolstoy, M., Harding, A.J. & Orcutt, J.A., 1993. Crustal thickness on the Mid-Atlantic Ridge: bull's-eye gravity anomalies and focused accretion, *Science,* **262**(5134), 726–729.

Van Avendonk, H.J.A., Hayman, N.W., Harding, J.L., Grevemeyer, I., Peirce, C. & Dannowski, A., 2017. Seismic structure and segmentation of the axial valley of the Mid-Cayman Spreading Centre, *Geochem. Geophys. Geosyst.,* **18,** 2149–2161.

Wessel, P. & Smith, W., 1998. New, improved version of Generic Mapping Tools released, *EOS, Trans. Am. geophys. Un.,* **79,** 579.

White, R.S., 1979. Oceanic upper crustal structure from variable angle seismic reflection-refraction profiles, *Geophys. J. R. astr. Soc.,* **57,** 683–726.

White, R.S., 1984. Atlantic Ocean crust: seismic structure of a slow spreading ridge, in *Ophiolites and Oceanic Lithosphere,* Vol. **13,** pp. 34–44, eds Gass, I.G., Lippard, S.J. & Shelton, A.N., Geol. Soc. Lond. Spec. Pub.

White, R.S. *et al.*, 1984. Anomalous seismic crustal structure of oceanic fracture zones, *Geophys. J. R. astr. Soc.,* **79**(3), 779–798.

White, R.S., Mckenzie, D. & O'Nions, R.K., 1992. Oceanic crustal thickness from seismic measurements and rare earth element inversions, *J. geophys. Res.,* **97,** 683–715.

White, R.S., Minshull, T.A., Bickle, M.J. & Robinson, C.J., 2001. Melt generation at very-slow spreading oceanic ridge: constraints from geochemical and geophysical data, *J. Petrol.,* **42**(6), 1171–1196.

Zelt, C.A., 1998. Lateral velocity resolution from three-dimensional seismic refraction data, *Geophys. J. Int.,* **135,** 1101–1112.

Zelt, C.A. & Barton, P.J., 1998. Three-dimensional seismic refraction tomography: a comparison of two methods applied to data from the Faeroe Basin, *J. geophys. Res.,* **103,** 7187–7210.

Zelt, C.A. & Ellis, R.M., 1988. Practical and efficient ray-tracing in two-dimensional media for rapid traveltime and amplitude forward modelling, *Can. J. Explor. Geophys.,* **21,** 16–31.

Zelt, C.A. & Smith, R.B.,1992. Seismic traveltime inversion for 2-D crustal velocity structure, *Geophys. J. Int.,* **108,** 16–34.

Zelt, C.A., Sain, K., Naumenko, J.V. & Sawyer, D.S., 2003. Assessment of crustal velocity models using seismic refraction and reflection tomography, *Geophys. J. Int.,* **153,** 609–626.

SUPPORTING INFORMATION

Supplementary data are available at *GJI* online.

Figure S1. Inversion modelling starting with the *seabed following initial model* (*cf.* Fig. 4). (a) Initial model. (b) Phase 1 interim model. (c) Final model. See text and Table 1 for approach and parameters adopted. χ^2 fit, the root-mean-square misfit (T_{RMS}) and the number of traveltime picks are labelled for each stage. Velocity contours are plotted at 1.0 km s^{-1} intervals, together with the 7.5 km s^{-1} contour used as a proxy for base of crust. (d) Cell hit count. In all parts, OBS locations are marked by inverted black triangles, with OBSs 001, 113 and 125 highlighted in red.

Figure S2. Inversion modelling starting with the *sloping bottom initial model* (*cf.* Fig. 4). (a) Initial model. (b) Phase 1 interim model. (c) Final model. See text and Table 1 for approach and parameters adopted. χ^2 fit, the root-mean-square misfit (T_{RMS}) and the number of traveltime picks are labelled for each stage. Velocity contours are plotted at 1.0 km s^{-1} intervals, together with the 7.5 km s^{-1} contour used as a proxy for base of crust. (d) Cell hit count. In all parts, OBS locations are marked by inverted black triangles, with OBSs 001, 113 and 125 highlighted in red.

Please note: Oxford University Press is not responsible for the content or functionality of any supporting materials supplied by the authors. Any queries (other than missing material) should be directed to the corresponding author for the paper.